

48

SATELLITE & MESOMETEOROLOGY RESEARCH PROJECT

Department of the Geophysical Sciences
The University of Chicago

A PROPOSED METHOD OF ESTIMATING CLOUD-TOP TEMPERATURE,
CLOUD COVERS, EMISSIVITY, AND CLOUDNESS FROM
SHORT- AND LONG-WAVE RADIATION DATA OBTAINED
BY MEDIUM-RESOLUTION SCANNING RADIOMETERS

by

Tetsuya Fujita and Hector Grandoso

FACILITY FORM 602

N68-16920
(ACCESSION NUMBER)

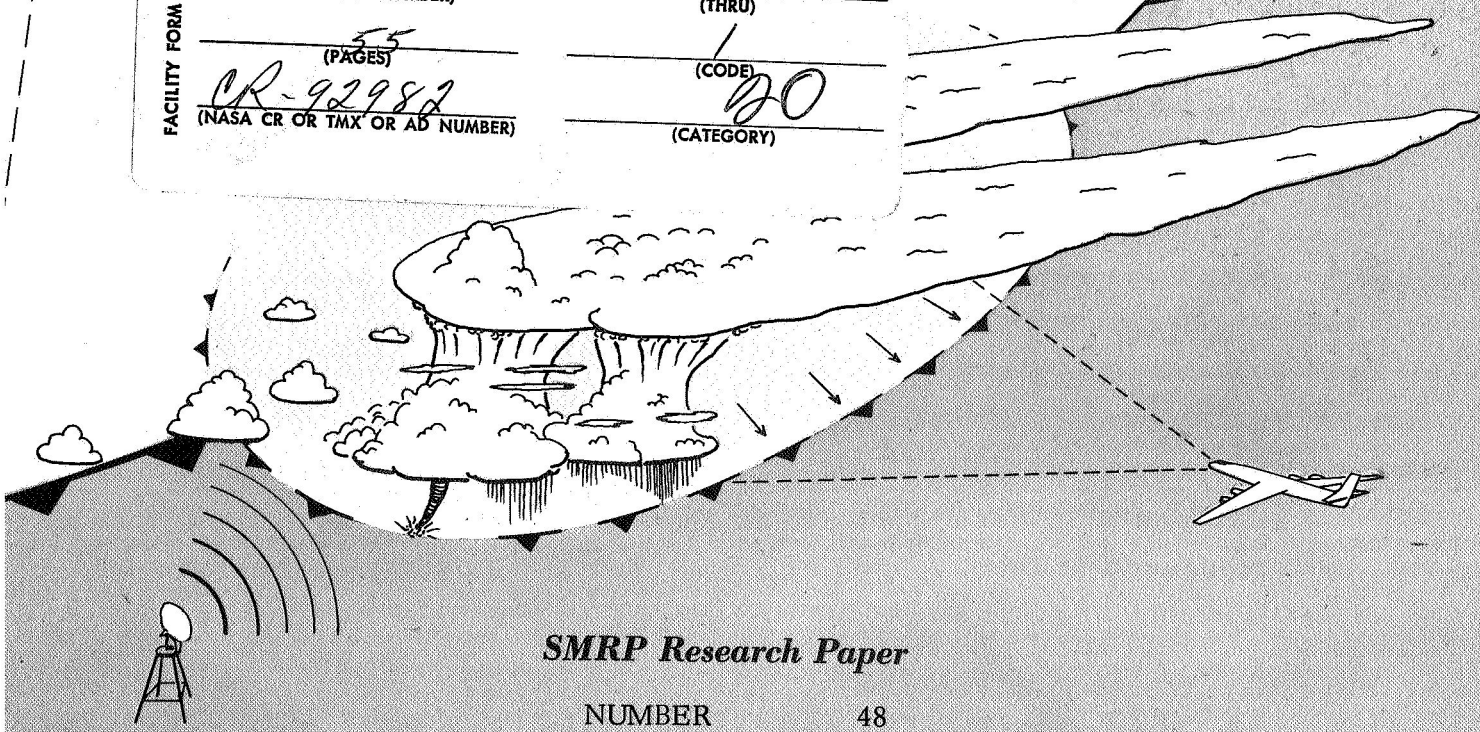
55
(PAGES)

CR-92982
(NASA CR OR TMX OR AD NUMBER)

(THRU)

1
(CODE)

20
(CATEGORY)



SMRP Research Paper

NUMBER 48
November 1967

SATELLITE AND MESOMETEOROLOGY RESEARCH PROJECT

Department of the Geophysical Sciences

The University of Chicago

A PROPOSED METHOD OF ESTIMATING CLOUD-TOP TEMPERATURE,
CLOUD COVERS, EMISSIVITY, AND CLOUDNESS FROM
SHORT- AND LONG-WAVE RADIATION DATA OBTAINED
BY MEDIUM-RESOLUTION SCANNING RADIOMETERS

by

Tetsuya Fujita and Hector Grandoso

SMRP Research Paper No. 48

November 1967

The research reported in this paper has been sponsored by the Meteorological Satellite Laboratory under Grant Cwb WBG-34 and by the National Aeronautics and Space Administration under Grant NsG-333.

TABLE OF CONTENTS

	Page
1. Introduction	2
2. Spectral and Spatial Responses of a Radiometer	4
3. Long-Wave Radiation from Clouds and Background in the Window Regions	7
4. Short-Wave Radiation from Clouds and Background	9
5. Emissivity, Reflectance, and Whiteness of Clouds	14
6. Equivalent Reference Cloud Cover	17
7. Computation of Effective Radiant Emittance of Clouds and Cloudness*	18
8. Computation of Equivalent Blackbody, Equivalent Reference, and Photographic Cloud Cover	21
9. Computation of Cloud Emissivity and Cloud Reflectance	23
10. Mapping Procedure for Estimating \bar{A}_b , $\tilde{\rho}_R^\bullet$, and \bar{W}_{Bb}	24
11. Effects of Sensor Degradation on Computation of Cloud Parameters	25
12. Application to the Meteorological Interpretation of Radiation Data	27
13. Conclusions	33

* Defined in this report, p. 1

LIST OF SYMBOLS

a	extinction coefficient
\bar{A}	effective albedo
b	as subscript indicates background
B	radiant emittance of a blackbody leaving the source
B	as subscript indicates blackbody
c	as subscript indicates cloud
C	cloudiness
g	degradation factor of long-wave sensor
h	degradation factor of short-wave sensor
i	error factor of photographic cloud cover
k	correction factor of extinction
n	radiometric cloud cover
n_B	equivalent blackbody cloud cover
n_p	photographic cloud cover
n_R	equivalent reference cloud cover
n_U	equivalent whitebody cloud cover
N	spectral radiance reaching a satellite sensor
\bar{N}	effective spectral radiance
R	as subscript indicates reference cloud
T_{BB}	equivalent blackbody temperature
T_{Bc}	equivalent blackbody cloud temperature
U	spectral radiant emittance of a whitebody leaving the source
U	as a subscript indicates whitebody
\bar{W}	effective radiant emittance reaching a satellite sensor
W^*	solar spectral radiant emittance reaching the top of the atmosphere
\bar{W}^*	effective solar radiant emittance reaching the top of the atmosphere
ϵ	emissivity of cloud
ζ	zenith angle
λ	wavelength
$\bar{\pi}$	effective pseudo-radiant emittance
ρ	reflectance of cloud
τ	transmissivity
ϕ_λ	spectral response of a sensor

ϕ_{Ω} spatial response of a sensor
 ψ scattering angle
 ω whiteness of cloud
 Ω solid angle

- as subscript indicates sea level
- as superscript indicates toward the satellite
- * as superscript indicates from the sun
- as superscript indicates effective value of a quantity filtered by a sensor's spectral response
- ~ as superscript indicates mean value
- = as superscript indicates the measured value of a quantity with — as a superscript and affected by a sensor's degradation
- ≈ as superscript indicates the mean value of a quantity affected by degradation or error of sensors

A PROPOSED METHOD OF ESTIMATING CLOUD-TOP TEMPERATURE,
CLOUD COVERS, EMISSIVITY, AND CLOUDNESS FROM
SHORT- AND LONG-WAVE RADIATION DATA OBTAINED
BY MEDIUM-RESOLUTION SCANNING RADIOMETERS¹

by

Tetsuya Fujita and Hector Grandoso
Department of the Geophysical Sciences
The University of Chicago
Chicago, Illinois

ABSTRACT

Despite the fact that the radiation data obtained by medium-resolution scanning radiometers are widely used in meteorology, their applications to mesoscale meteorological phenomena are still hampered because their field of view is large compared to the horizontal dimensions of the clouds to be investigated. With the knowledge that the basic approach to the interpretation of radiation data varies significantly according to the horizontal dimensions of the meteorological systems under investigation, a complete analysis of radiation data has been attempted taking into consideration the spatial response of the sensors and cloud cover inside their field of view. It was revealed that the cloud cover observed varied according to the spectral responses of the radiometers, thus necessitating the establishment of radiometric cloud covers which can be identified as the equivalent reference cloud cover (smallest), the equivalent blackbody cloud cover, and the photographic cloud cover (largest). It was found that the ratio of the first and second cloud covers for faint cirrus clouds is very small, but increases to 1.0 as the clouds become denser and thicker. Thus this ratio, which can be used to identify clouds, is called the "cloudness" which is in fact not "cloudiness." A method of determining the cloud emissivity was also obtained by solving general radiometric equations involving a two-radiance model. Test analyses revealed that the emissivity of cirrus clouds ranges between 0.0 and 1.0 when a 10-micron channel is used. If cirrostratus or an anvil cloud appears very bright in a satellite picture,

¹The research reported in this paper has been sponsored by the Meteorological Satellite Laboratory under Grant Cwb WBG-34 and by the National Aeronautics and Space Administration under Grant NsG-333.

we may safely assume that its emissivity is very close to 1.0. When high clouds appear rather faint in a picture, the emissivity of these clouds varies between 0.4 and 0.7. A high cloud with emissivity of less than 0.3 is not always recognizable in TIROS pictures. As a result of this study, it became evident that the equivalent blackbody temperatures from Medium Resolution Radiation data cannot always be used as the cloud-top temperatures because of the varying emissivity of clouds and their partial coverage of the radiometer's field of view.

1. Introduction

Since the Medium Resolution Scanning Radiometers on board the TIROS II meteorological satellite first measured terrestrial radiation, their potential use in determining the radiative characteristics of the earth and its atmosphere has been discussed on various occasions.

Nordberg, Bandeen, Conrath, Kunde, and Persano (1962) introduced a pioneering work on the mapping of radiative characteristics of clouds and cloud-free ground. Since then, the Grid Print Maps in various scales and the Final Meteorological Radiation Tapes have become available to meteorologists whose research interests cover nephsystems with horizontal dimensions customarily described in terms of micro-, meso-, and macroscale. Because the horizontal resolution of the Medium Resolution Radiation (MRR) data is limited by scan-spot sizes, it is almost hopeless to obtain microscale radiation patterns from them. Mesoscale patterns are on the borderline of mapping feasibility. The Grid Print Maps in 1:20,000,000 or smaller scales represent macroscale radiation patterns affected by synoptic and planetary meteorological disturbances.

It should be pointed out, however, that the Grid Print Maps in their standard forms give patterns of effective radiant emittances or corresponding equivalent blackbody temperatures. These patterns by themselves do not give separate information about cloud temperatures and cloud cover because their particular combinations would result in an identical effective radiant emittance. The first attempt to deduce effective cloud heights and percentage of cloud cover was made by Rasool (1964). The results of his computation rely heavily on the assumption that reasonably thick clouds are practically opaque to 4μ or longer infrared radiation, but he applied this assumption to all clouds.

When this assumption is made in solving for the basic cloud parameters of mesoscale nephsystems, the partial filling of a scan spot by clouds and the emissivity of the clouds must be taken into consideration. In his experiment in objective nephanalysis using simulated HRIR data, Maykut (1964) made an attempt to obtain cloud cover through

an automatic comparison of the temperature field at three reference heights and equivalent blackbody temperatures converted from the well-known equation of effective radiant emittance,

$$\bar{W} = \int_0^{\infty} W_{\lambda(T)} \phi_{\lambda} d\lambda$$

It must be kept in mind that this is the equation for obtaining the effective radiant emittance from a blackbody radiator filling the entire field of view. Actual clouds with emissivity ϵ that fill x part of the radiometer's field of view would give an effective radiant emittance

$$\bar{W}_{\text{CLOUD}} = \int_0^{\infty} \epsilon x W_{\lambda(T_c)} \phi_{\lambda} d\lambda$$

where T_c denotes the radiative temperature of the cloud. This effective radiant emittance will be mixed with that from the background within the field of view before being detected by a radiometer, resulting in a considerable difference between the measured \bar{W} and that which would be measured if the clouds were opaque radiators and covered the entire field of view. For HRIR data, x will be close to 1.0 in more cases than for MRR data; however, emissivity measurements made by Brewer and Houghton (1956), Gates and Shaw (1960), and Kuhn (1963), for instance, clearly indicate that high, thin clouds are far from being blackbody radiators. This indicates that a low emissivity combined with only partial filling of the radiometer's field of view might result in a serious misinterpretation when Maykut's cloud covers, especially above 20,000 and 30,000 ft, are used operationally. For example, an extensive area of jet-stream cirrus might turn out to be that of middle, overcast clouds.

This fact does not mean that MRR and HRIR data cannot be used in differentiating high clouds from middle and low ones. As demonstrated by Whitney (1965), a narrow zone of Channel 2 temperature gradient, -38°C (12 CPS) to -27°C (15 CPS), coincided with a long shadow of jet-stream cirrus. Combined analysis of MRIR data, appearance of high clouds in pictures, and aerological data permitted him to draw a reasonable conclusion with regard to the split-level cloud structure.

Since we do not yet entirely know the radiative properties of clouds observed by scanning radiometers, solutions of basic problems are necessary before a realistic objective method of computing cloud height, cloud cover, etc., can be established. In order to obtain the cloud cover from radiation data, Wexler (1964) proposed the simple formulae

$$C' = \frac{A - A_o}{A_c - A_o} \quad \text{and} \quad C' = \frac{I_o - I}{I_o - I_c}$$

where C' denotes the cloud cover; A , the measured albedo; I , the measured Channel 2 intensity; and suffixes c and o designate the cloud and the background, respectively. When the authors made test analyses of cloud covers using Wexler's formulae, it was found that the cloud covers computed from infrared data always had higher values than those from short-wave data, especially when high cirriform clouds were involved. This fact leads to the very important conclusion that the cloud covers vary according to the spectral responses of the radiometers.

Another important fact revealed by further studies of cloud covers is that the infrared cloud cover of relatively thin, cirriform clouds turns out to be extremely small when computed by one of Wexler's formulae, even though satellite photographs show that the clouds are much larger than the radiometer's field of view. This evidence necessitates a clear distinction between the radiometric and the conventional cloud covers.

The authors, therefore, concluded that it is important to first distinguish the basic cloud parameters that are combined into the effective radiant emittances measured by the radiation sensors, then to derive equations to calculate these basic parameters from measured effective radiant emittances. In doing this, however, proper calibration of the radiometers must take into consideration degradation as a function of orbit numbers.

As shown in NASA's (1961-64) TIROS Radiation Data User's Manuals, degradation of MRR sensors always exists. Fritz, Krishna Rao, and Weinstein (1964) pointed out that we have to be aware of uncertainty in the values of degradation correction for short-wave sensors. Infrared sensors are also affected by degradation, but this can be corrected with reasonable accuracy. In the development of equations, therefore, short-wave data were used only in the form of ratios so that the uncertainty in degradation correction does not alter the computed results.

2. Spectral and Spatial Responses of a Radiometer

Medium Resolution Radiometers (MRR) on board TIROS and Nimbus meteorological satellites sense the radiant energy falling on their detector surfaces. In order to obtain the radiant emittance within certain spectral ranges and within a small solid angle of view around the radiometer axis, each radiometer is characterized by both spectral response, ϕ_λ , and spatial response, ϕ_Ω . The former, which varies with both TIROS and channel numbers, is given in NASA's Users' Manuals (1961-64), but the latter, for TIROS MRR, is designed to be about a 5° cone at half-power response. A schematical drawing of a radiometer in Fig. 1 shows that the radiant energy from an area element,

dS , on the earth is focused on the detector surface to generate an output power, dP . If we assume that this output power is equal to the input power filtered through spectral and spatial responses, it can be written as

$$dP = N_{\lambda} M D^{-2} \phi_{\lambda} \phi_{\Omega} dS_n d\lambda , \quad (1)$$

where M denotes the area of the lens; D , the distance from the lens to the area element, dS ; and N_{λ} , the spectral radiance reaching the sensor from dS_n , which represents the normal component of the area, dS , viewed from the satellite. In order to simplify the notation, the subscript λ , meaning wave-length dependent, will be dropped from the spectral radiance as well as from the radiant emittance, emissivity, transmissivity, and reflectance. After rearranging Eq. (1), we integrate the output power as

$$\begin{aligned} P &= \iint N_{(\Omega)} M \phi_{\lambda} \phi_{\Omega} \frac{dS_n}{D^2} d\lambda \\ &= M \iint N_{(\Omega)} \phi_{\lambda} \phi_{\Omega} d\Omega d\lambda , \end{aligned} \quad (2)$$

where $dS_n / D^2 = d\Omega$ represents the solid angle of dS_n or dS viewed from the satellite. It should be noted that a unique output power can be computed only if N_{λ} is given as a function of both λ and Ω . Thus the output power varies when a small cloud of identical spectral radiance is located in different parts of a radiometer's field of view.

By definition, the spatial response, ϕ_{Ω} , is the ratio of input and output powers when the incoming radiant energy is focused on various parts of the detector surface. An example of non-circular distribution of spatial response contoured with percent-power lines appears in Fig. 2. The degree scales on the x and y axes denote radial angles measured from the radiometer axis. It is seen that the spatial response drops to 50% when the radial angle exceeds about 3° , while the isoline of zero response extends to about 7° , indicating that a MRR integrates radiant energy within a cone of about 15° vertex angle with its half-power extending to about 5° .

Since the output power and the spectral radiance inside the field of view cannot be related unless N_{λ} is known as a function of λ and Ω , NASA (1961-64) calibrated all radiometers under laboratory conditions such that N was constant everywhere inside the field of view. This condition is, of course, far from realistic when applied to actual observations, because the field of view projected on the earth is larger than a circle of 50-km diameter. Users must, therefore, fully realize this basic characteristic of the calibration so that a reasonable interpretation of radiation data can be made under various meteorological situations and research requirements. For NASA's calibration

purposes, the right side of Eq. (2) can be reduced to

$$P = M \int \phi_{\Omega} d\Omega \int N \phi_{\lambda} d\lambda = M_0 \bar{N} ,$$

where $M_0 = M \int \phi_{\Omega} d\Omega$ and $\bar{N} = \int N \phi_{\lambda} d\lambda$. (3)

M_0 is a quantity unique to each radiometer; however; it is not necessary to determine its value since P can be related to \bar{N} through pre-launch calibration. The quantity \bar{N} is called the effective radiance and represents the integrated radiance reaching the sensor within its spectral response. If we assume isotropic radiation, \bar{N} can be converted into \bar{W} , the effective radiant emittance, using the formula, $\bar{W} = \pi \bar{N}$.

Putting Eqs. (2) and (3) together, we obtain the equation of \bar{N} ,

$$\bar{N} = \iint N_{(\Omega)} \phi_{\lambda} \phi_{\Omega} d\Omega d\lambda / \int \phi_{\Omega} d\Omega . \quad (4)$$

This equation cannot be reduced any further unless specific models of cloud distribution are established.

Multi-radiance Model. In this generalized model we assume that a finite number of radiatively identical clouds can be grouped into one. These clouds may be characterized by any emissivity and albedo values as long as they do not vary within each group. Identifying these cloud groups by $c_1, c_2, c_3, \dots, c_j$ and background groups by $b_1, b_2, b_3, \dots, b_i$, we have

$$\int d\Omega = \int d\Omega_{c_1} + \dots + \int d\Omega_{c_j} + \int d\Omega_{b_1} + \dots + \int d\Omega_{b_i} . \quad (5)$$

We can then express the radiance from these cloud areas by N_c , which represents the mixed radiation from the cloud and the background when the emissivity or albedo is less than one. No radiation exclusively from a cloud can be measured by a radiometer unless it is 100% white (short wave) or 100% black (long wave). N_b , on the other hand, consists of the radiance from background areas entirely free of clouds. Both N_c and N_b include, by definition, the effects of atmospheric absorption and scattering, inside the field of view. Now we rewrite Eq. (4) in the form,

$$\bar{N} = \left[\sum_j \int \phi_{\Omega} d\Omega_{c_j} \int N_{c_j} \phi_{\lambda} d\lambda + \sum_i \int \phi_{\Omega} d\Omega_{b_i} \int N_{b_i} \phi_{\lambda} d\lambda \right] / \int \phi_{\Omega} d\Omega , \quad (6)$$

which denotes that the effective radiance, \bar{N} , is the weighted mean radiance from both cloud and background in groups. A general solution of this equation cannot be obtained since too many variables are involved.

Two-Radiance Model. Although the distribution of N within the field of view cannot always be separated into two groups, each with uniform radiative properties, the one-radiance model can be improved significantly. In this model, we shall assume that

$$N_c = N_{c_1} = N_{c_2} = \dots \dots N_{c_j}$$

and

$$N_b = N_{b_1} = N_{b_2} = \dots \dots N_{b_i}$$

thus allowing the coexistence of radiance from the areas of both clouds and background.

When applied to this model, Eq. (6) is reduced to

$$\bar{N} = \frac{\int \phi_{\Omega} d\Omega_c}{\int \phi_{\Omega} d\Omega} \int N_c \phi_{\lambda} d\lambda + \frac{\int \phi_{\Omega} d\Omega_b}{\int \phi_{\Omega} d\Omega} \int N_b \phi_{\lambda} d\lambda, \quad (7)$$

which can be expressed in a very simple form,

$$\bar{N} = n\bar{N}_c + (1-n)\bar{N}_b, \quad (8)$$

where \bar{N}_c and \bar{N}_b denote the effective radiance from the areas of clouds and background, respectively; n , expressed by

$$n = \int \phi_{\Omega} d\Omega_c / \int \phi_{\Omega} d\Omega, \quad (9)$$

is called the "radiometric cloud cover," and represents the weighted sum of the solid-angle elements filled with clouds divided by those inside the entire field of view. Thus the radiometric cloud cover within a field of view varies when the same cloud is moved from one location to the other because ϕ_{Ω} is not the same everywhere.

In order to integrate the spatial response inside solid-angle elements filled with cloud, it is necessary to identify the solid-angle elements which are cloud-filled. Since the detectability of a cloud is a function of the spectral response of a sensor, the radiometric cloud cover of the same cloud varies with the spectral response. For instance, the radiometric cloud cover within the visual spectral range would decrease considerably when measured with 10-cm radar having the identical spatial response. On the contrary, invisible cirrus could be detected by a proper infrared sensor.

3. Long-Wave Radiation from Clouds and Background in the Window Regions

The spectral radiance of a blackbody radiator is given by B/π at the source since a blackbody is assumed to radiate isotropically by definition. The quantity, B , is the spectral radiant emittance expressed by Planck's law of blackbody radiation. When the spectral radiant emittance is measured from outer space, it is written as

$$N = \frac{B}{\pi} \tau_{\text{sfc}}^{\bullet} + \frac{1}{\pi} \int_{\tau_{\text{sfc}}^{\bullet}}^{\tau=1} B_{(\tau)} d\tau^{\bullet} \quad , \quad (10)$$

where N denotes the spectral radiant emittance from the blackbody surface, $\tau_{\text{sfc}}^{\bullet}$ denotes the spectral transmissivity of the atmosphere from the surface toward the satellite, and the integral in the second term on the right side of the equation represents the radiance of the atmosphere between the surface and the satellite.

As long as we consider infrared radiation in the window channels, we may assume $\tau^{\bullet} = 1$, thus permitting us to drop the contribution of the atmosphere.

Now we shall assume that the radiometer's field of view is occupied by a radiometric cloud cover, n , defined by Eq. (9). The rest of the field of view, $1 - n$, constitutes the background. Since the background is the earth, it can be assumed to be a blackbody, thus

$$\bar{N}_b = \int \phi_{\lambda} N_b d\lambda = \int \phi_{\lambda} \frac{B_b}{\pi} d\lambda = \frac{\bar{W}_{B_b}}{\pi} \quad , \quad (11)$$

where B_b denotes the spectral radiant emittance of the background at the source and \bar{W}_{B_b} , the effective radiant emittance of the background measured through the atmosphere.

To generalize the computation, the spectral emissivity of the cloud is expressed by ϵ , which may vary between 0.0 and 1.0. Thus the cloud may not radiate as a blackbody and the radiation from the background beneath the cloud partially penetrates the cloud. The effective radiance from the areas of clouds can now be written as

$$\begin{aligned} \bar{N}_c &= \int \phi_{\lambda} N_c d\lambda \\ &= \int \phi_{\lambda} \epsilon \frac{B_c}{\pi} d\lambda + \int \phi_{\lambda} (1 - \epsilon) \frac{B_b}{\pi} d\lambda \\ &= \frac{\tilde{\epsilon}}{\pi} \int \phi_{\lambda} B_c d\lambda + \frac{1 - \tilde{\epsilon}}{\pi} \int \phi_{\lambda} B_b d\lambda \\ &= \frac{\tilde{\epsilon}}{\pi} \bar{W}_{B_c} + \frac{1 - \tilde{\epsilon}}{\pi} \bar{W}_{B_b} \end{aligned} \quad (12)$$

where B_c denotes the spectral radiant emittance of a blackbody replacing the actual cloud; $\tilde{\epsilon}$, the mean emissivity of the cloud; and \bar{W}_{B_c} and \bar{W}_{B_b} denote the effective radiant emittances corresponding to the temperatures of the cloud top and the background as measured at the satellite.

Equations (11) and (12) are then added in the form of Eq. (8) after multiplying by n and $(1 - n)$, respectively. Thus

$$\bar{N} = n \left(\frac{\tilde{\epsilon}}{\pi} \bar{W}_{B_c} + \frac{1 - \tilde{\epsilon}}{\pi} \bar{W}_{B_b} \right) + (1 - n) \frac{\bar{W}_{B_b}}{\pi} \quad ,$$

which is reduced to a simple equation

$$\bar{W} = n \tilde{\epsilon} \bar{W}_{B_c} + (1 - n \tilde{\epsilon}) \bar{W}_{B_b}, \quad (13)$$

where $\bar{W} = \pi \bar{N}$ is the effective radiant emittance measured at the satellite. When a sensor measures radiation from a large area of clouds with mean emissivity $\tilde{\epsilon}$, we have

$$\bar{W} = \tilde{\epsilon} \bar{W}_{B_c} + (1 - \tilde{\epsilon}) \bar{W}_{B_b}. \quad (14)$$

It should be noted that the measured effective radiant emittance cannot be interpreted as that of a cloud which has been assumed to be a blackbody. Thin cirrus or cirro-stratus clouds almost always have an emissivity less than 1.0. When the cloud cover formed by such clouds is extensive in relation to the field of view, the mapped effective radiant emittances often represent the "emissivity distribution" rather than the pattern of "cloud-top temperature."

Equivalent Blackbody Cloud Cover. Not all clouds may be considered blackbodies, so it is convenient to introduce a cloud cover $n_B = \tilde{\epsilon} n$, in order to write

$$\bar{W} = n_B \bar{W}_{B_c} + (1 - n_B) \bar{W}_{B_b} \quad (15)$$

where n_B , called the "equivalent blackbody cloud cover," represents the cover of a hypothetical blackbody cloud which radiates the same amount of radiation as is emitted by the actual clouds inside the field of view. The temperatures of the hypothetical and actual clouds are assumed to be identical. Thus the equivalent blackbody cloud cover is far less than 1.0, especially when cirriform clouds are involved.

4. Short-Wave Reflection from Clouds and Background

An actual cloud reflects incoming solar radiation as a diffuse reflector, not as a perfectly diffuse reflector which reflects isotropically the radiant energy incident upon the surface. It is known that a deck of stratified clouds reflects somewhat like a specular reflector, especially for a high solar zenith angle. When cloud tops are illuminated from directly above, however, they reflect the incoming radiation more or less isotropically.

We shall, first of all, define a "whitebody" as a perfectly diffuse reflector with spectral reflectance, ρ_0 , equal to 1.0 throughout the entire spectral range. Thus, a

whitebody diffuses isotropically the total radiant energy incident upon its surface. The spectral radiant emittance of a whitebody illuminated by the sun with its zenith angle ζ^* can therefore be written as

$$U = W^* \tau^* \cos \zeta^* ,$$

where W^* denotes the solar spectral radiant emittance reaching the top of the atmosphere, and τ^* , the transmissivity of the atmosphere from the sun to the whitebody. The spectral radiance emitted from this whitebody that reaches the satellite can be written as

$$N_u = \frac{W^*}{\pi} \tau^* \tau^\circ \cos \zeta^* \quad (16)$$

because a whitebody emits isotropically.

The background is assumed to be a diffuse reflector with spectral reflectance, ρ_b° , which varies according to the direction of measurement as well as the wave length. The effective radiance of the background can be obtained by integrating the spectral radiance from the whitebody to the satellite N_{ub} , after multiplying by ϕ_λ and ρ_b° ; thus

$$\bar{N}_b = \int N_{ub} \rho_b^\circ \phi_\lambda d\lambda . \quad (17)$$

The effective radiance from the region of clouds consists of the energy reflected from the clouds and that reflected from the background, and reaches the radiometer after penetrating the clouds. The former can be written as

$$\bar{N}_{c1} = \int N_{uc} \rho^\circ \phi_\lambda d\lambda , \quad (18)$$

where N_{uc} represents the spectral radiance of a whitebody placed at the cloud height and ρ° , the spectral reflectance of actual clouds. The latter is rather complicated, because the radiation penetrating the cloud toward the satellite comes from the background. Neglecting the absorption, we write

$$\bar{N}_{c2} = \int N_{ub} (1 - \rho^\circ) \rho_b^\circ \phi_\lambda d\lambda , \quad (19)$$

where N_{ub} represents the spectral radiance from a whitebody placed at the background height and ρ_b° , the spectral reflectance of the actual background in the direction of the satellite.

Expressing the mean reflectance of cloud and background within the spectral range of the sensor, ϕ_λ , by $\tilde{\rho}^\circ$ and $\tilde{\rho}_b^\circ$ respectively, Eq. (17), (18), and (19) are reduced, respectively, to

$$\bar{N}_b = \tilde{\rho}^* \bar{N}_{Ub} \quad (20)$$

$$\bar{N}_{C1} = \tilde{\rho}^* \bar{N}_{Uc} \quad , \quad (21)$$

and
$$\bar{N}_{C2} = (1 - \tilde{\rho}^*) \bar{N}_b \quad , \quad (22)$$

where $\tilde{\rho}^*$, the mean reflectance, is defined by

$$\tilde{\rho}^* = \frac{\int N \rho^* \phi_\lambda d\lambda}{\int N \phi_\lambda d\lambda} .$$

After multiplying the cloud cover, n , by $(\bar{N}_{C1} + \bar{N}_{C2})$ and $(1 - n)$ by \bar{N}_b , we write

$$\bar{N} = n(\bar{N}_{C1} + \bar{N}_{C2}) + (1 - n)\bar{N}_b \quad ,$$

and after substituting Eq. (20), (21), and (22),

$$\bar{N} = n\tilde{\rho}^* \bar{N}_{Uc} + (1 - n\tilde{\rho}^*) \bar{N}_b \quad . \quad (23)$$

Multiplying both sides by $\pi/\bar{W}^* \cos \zeta^*$ to obtain the effective albedos,

$$\bar{A} = n\tilde{\rho}^* \bar{A}_{Uc} + (1 - n\tilde{\rho}^*) \bar{A}_b \quad , \quad (24)$$

where $\bar{A} = \pi \bar{N} / \bar{W}^* \cos \zeta^*$, $\bar{A}_{Uc} = \pi \bar{N}_{Uc} / \bar{W}^* \cos \zeta^*$, and $\bar{A}_b = \pi \bar{N}_b / \bar{W}^* \cos \zeta^*$ are, respectively, the albedo measured at the satellite, the albedo of a whitebody replacing the actual cloud, and the albedo of the background. If the satellite measures the albedos of the same area from other directions, they would vary according to the zenith angles of the sun and the satellite, as well as the scattering angle. Furthermore, Eq. (24) shows that the measured albedo is a mixture representing the areas of clouds and background.

Equivalent Whitebody Cloud Cover. Following the same procedure as for defining n_b in Eq. (15), we write Eq. (24) in the form

$$\bar{A} = n_u \bar{A}_{Uc} + (1 - n_u) \bar{A}_b \quad , \quad (25)$$

where $n_u = \tilde{\rho}^* n$ is called the "equivalent whitebody cloud cover." Unlike the case for equivalent blackbody, n_u could be larger than n , the actual cloud cover, because $\tilde{\rho}^*$ may exceed 1.0 when the reflection is highly specular. In most cases, however, n_u may be considerably less than the actual cloud cover since the reflectance of clouds is usually less than 1.0.

Albedo of Whitebody Cloud. The albedo of a whitebody cloud depends upon the

cloud height and the radiative properties of the atmosphere in which the whitebody cloud is embedded. It should be noted, however, that the albedo reaches 1.0 when a whitebody cloud is brought to the top of the atmosphere. From Eq. (16) and the definition of albedo in Eq. (24), we express A_{uc} , the albedo of a whitebody placed at the cloud top height, as

$$\begin{aligned}\bar{A}_{uc} &= \pi \bar{N}_{uc} / \bar{W}^* \cos \zeta^* = \pi \int N_{uc} \phi_\lambda d\lambda / \bar{W}^* \cos \zeta^* \\ &= \frac{1}{\bar{W}^*} \int W^* \tau_c^* \tau_c^\circ \phi_\lambda d\lambda \\ &= \overline{\tau_c^* \tau_c^\circ} = 1 - a_c ,\end{aligned}\tag{26}$$

where a_c is the extinction coefficient along the optical path from the sun to the cloud to the satellite. The transmissivity from the sun should include the sky radiation. However, τ_c° is practically free from sky radiation because the field of view of the sensor under discussion is small.

When the whitebody is located at sea level, the effective albedo can be written simply by changing the suffixes "c" in Eq. (26) into "o" which designates the sea level. Thus, we have

$$\bar{A}_{uo} = \overline{\tau_o^* \tau_o^\circ} = 1 - a_o \tag{27}$$

where a_o , called the "extinction coefficient at sea level," can be computed as a function of τ_o^* and τ_o° for a given atmosphere. Since it is not feasible to compute a_o for all possible atmospheres, it was decided to use Table 148 in the Smithsonian Meteorological Tables (1958), which gives the spectral distribution of solar radiation at sea level after taking into consideration scattering by water vapor, air, dust, and the absorption by water vapor and ozone. The data in the table have been computed for an atmosphere with the following characteristics: water vapor, 20-mm precipitable water; dust, 300 particles cm^{-3} near the ground; and ozone, 2.8-mm path length at N.T.P. In order to compute the extinction coefficient from that table, the entire range of the solar radiation was divided into six spectral intervals, the optical airmass was converted to solar and satellite zenith angles, and the spectral response of the short-wave satellite sensor was taken into account. The relation between direct solar radiation and total solar and sky radiation in Table 150, Smithsonian Meteorological Tables, (1958), and the spectral distribution of the scattered solar radiation in the Handbook of Geophysics (1961) are used in computing the sky radiation for these six spectral intervals.

The extinction coefficient obtained by changing both solar and satellite zenith angles between zero and 80° is contoured in Fig. 3. These isolines represent the values

for the spectral response of the TIROS III, Channel 3, floor sensor. Nevertheless, they may be considered to represent approximately the values for other shortwave sensors. It is seen that the albedo decreases by almost 40% when both ζ^* and ζ° are zero. A combination of higher zenith angles gives a much larger extinction coefficient.

The planetary albedo when the whitebody cloud is brought to a higher altitude of pressure, p_c , is rather complicated. In order to compute the extinction coefficient as a function of the cloud-top pressure in addition to ζ^* and ζ° , it is necessary to know the vertical distribution of the Rayleigh scattering coefficients, the aerosol attenuation coefficients, and the atmospheric ozone absorption coefficients. Since it is not feasible to know these coefficients as a function of time and location, an attempt was made to determine a correction factor, k , after writing the extinction coefficient, a_c , at the cloud-top altitude with pressure, p_c , as

$$a_c = k a_o \frac{p_c}{p_o}$$

or $k = \frac{a_c p_o}{a_o p_c}$. (28)

The determining of k was done by computing extinction coefficients from Elterman's (1964) results, which give the vertical distribution of attenuation within the spectral region centered at 0.55 micron up to 50 km altitude. In order to cover the extreme angles of radiation measurements, a case with $\zeta^* = \zeta^\circ = 0$ and the other with $\zeta^* = \zeta^\circ = 60^\circ$ was calculated. Figure 3 represents the variation of the extinction coefficients from which the correction factor k shown below was obtained.

Table I. Values of k as a function of pressure and zenith angles.

Clouds	Low Clouds			Middle Clouds				High Clouds		
Pressure, mb	1000	900	800	700	600	500	400	300	200	100
0° Zenith Angle	1.00	0.75	0.61	0.53	0.50	0.50	0.50	0.50	0.50	0.50
60° Zenith Angle	1.00	0.82	0.70	0.69	0.61	0.60	0.60	0.60	0.60	0.60

The correction factor, k , thus obtained is fairly constant for middle and high clouds, and the change in the zenith angles from 0° to 60° does not alter the correction factor beyond the expected variation of attenuation characteristics from day to day. For practical purposes, therefore, k may be considered to be 0.6 unless extremely low clouds or sea fog are involved.

In order to determine a_c , the extinction coefficient from cloud-top altitude to the top of the atmosphere, the pressure at cloud-top altitude, p_c , has to be known in Eq. (28).

Fortunately, the effective radiant emittances of TIROS Channel 2 radiometers are such that we may approximate with a high degree of accuracy that

$$p_c/p_o = \bar{B}_c/\bar{B}_b = \bar{W}_{Bc}/\bar{W}_{Bb} \quad , \quad (29)$$

when pressure is converted into temperature of the standard atmosphere and the corresponding effective radiant emittance is then computed. This linear relationship between pressure and effective radiant emittance is shown in Fig. 5.

Using Eq. (26), (28), and (29), the effective albedo of a whitebody cloud located at cloud top level is

$$\bar{A}_{Uc} = 1 - a_c = 1 - k a_o \frac{\bar{W}_{Bc}}{\bar{W}_{Bb}} \quad (30)$$

5. Emissivity, Reflectance, and Whiteness of Clouds

The emissivity of clouds depends not only upon the size and the concentration of hydrometeors but also upon their shapes and states. A complete solution of cloud emissivity applicable to all types of clouds ranging from stratus to cirrus does not exist at the present time because of mathematical difficulties involving noncircular shapes of hydrometeors, especially those of ice clouds.

In an attempt to make very rough estimates of the emissivity of all clouds, McDonald's (1960) concept of computing the absorption by a water-film approach was used. In this approach, the absorption of infrared by a thin water film is assumed identical to that of a cloud produced by breaking the film into tiny droplets without changing the total mass. McDonald's estimate, made by taking the Mie theory into consideration, indicated that the water-film approach tends to yield absorptivities too low. Nevertheless, the bulk-water absorption depths give a fairly good idea as to the absorptivity of clouds as a function of the liquid water content and cloud thickness.

The left diagram of Fig. 6 gives the effective emissivity of clouds computed under a thin water-film assumption, in which

$$\bar{\epsilon} = \frac{\int \phi_\lambda e^{-\gamma f} B_{(\pi)} d\lambda}{\int \phi_\lambda B_{(\pi)} d\lambda} \quad , \quad (31)$$

where γ denotes the absorption coefficient converted from McDonald's decimal coefficient of absorption; f , the film thickness; B , the spectral radiant emittance from Planck's blackbody radiator; and ϕ_λ , the spectral response of a radiometer.

In computing the curves for 0.3, 0.1, and 0.06 g/m³ of liquid water content, w , cloud temperatures were increased from 200 K (-73C) to 300 K (+27C). The variation

in the emissivity due to this temperature increase of 100 C appeared to be negligibly small. In fact, the emissivity of clouds with $w = 0.3 \text{ gm}^{-3}$ increases to almost 1.0 at the 0.3-km depth below the cloud top. Fog and stratus clouds would be characterized by such a value of w . We may thus assume that convective clouds are radiatively black. Thick cirrostratus and altostratus clouds with $w = 0.1$ may be assumed to be black when their depth exceeds about 0.7 km or 2000 ft, while cirriform clouds with $w = 0.05$ must be over 1.0-km or 3000-ft thick in order to be regarded as blackbody radiators.

Reflection of shortwave radiation from actual clouds is more complicated than that from water-film which may be substituted for estimating longwave radiation from clouds. Since the wavelength is much smaller than most cloud drops, shortwave radiation reflects more as the reflective surface increases. As a result, a water film changes into a good reflector when it is broken into tiny cloud droplets. If we keep breaking these droplets without changing the total mass per unit area, it is expected that the reflectivity from the area will increase until the drop sizes and the wavelength become comparable.

In order to make a rough estimate of cloud albedoes in relation to liquid water content and drop sizes, Fritz's (1954) approach was used. First, we express the mean free path of light as

$$L = \frac{4}{3} \frac{r}{w} \quad , \quad (32)$$

where L denotes the mean free path in m; r , the mean radius of cloud droplets in microns, and w , the liquid water content in gm^{-3} . It is obvious that L increases in proportion to the drop radius for a given value of w , because the number of drops decreases in inverse proportion to the cube of the drop radius while the scattering cross-section increases in proportion to the square of the drop radius. Fritz's formula gives cloud albedo as a function of h/L , where h is the depth below the cloud top. The curves in Fig. 6 showing the change in albedo with increasing depth were computed from his formula when h/L is less than 10. Above this value, the reflectance was estimated from observational values by Bullrich (1948), Neiburger (1949), Fritz (1950), and Kikuti et al. (1954). Fritz's (1954) equation is not used when h/L exceeds 10, since the equation then gives values increasing to 1.0. Furthermore, computation for a cloud with thickness far beyond the mean free path is not justifiable, even though the transport mean free path applicable to actual clouds is known to be 2 to 4 times larger than the mean free path. A set of curves in the right diagram of Fig. 6 thus represents reasonable variations of the albedo of clouds with various liquid water contents and drop

radii. Of interest is the case with $w = 0.05$ and $r = 20$ micron, which would represent average high and thin clouds. The cloud albedo for such clouds increases very gradually with depth. When the drop size or the ice-crystal size is much larger than 20 microns, for example, 200 microns as frequently observed, the clouds of relatively small thickness cannot be seen by the naked eye, but might radiate long wave radiation.

It has been shown that cloud emissivity, as well as cloud albedo, increases with cloud depth. Because $\tilde{\epsilon}$ is usually larger than $\tilde{\rho}^*$, the ratio of the former divided by the latter increases as the cloud depth increases. The "whiteness" of clouds, defined by

$$\tilde{\omega}^* = \tilde{\rho}^* / \tilde{\epsilon} \quad (33)$$

and computed from Fig. 6, is shown in Fig. 7.

Despite the fact that the whiteness varies according to the direction of measurement and the cloud types, it reaches a saturation value when a cloud with liquid water content above 0.3 g/m^3 and with drops mostly less than 10 microns is more than 1 km thick. The figure indicates that the whiteness of relatively thick water clouds such as Cu, Cb, St, Sc, and fog reaches a saturation value when the thickness increases. This value, however, varies as a function of ζ^* and ζ° , the solar and satellite zenith angles, and as a function of $\Delta\alpha$, the relative azimuth. Thus,

$$\tilde{\rho}_R^* = f(\zeta^*, \zeta^\circ, \Delta\alpha) ,$$

where $\tilde{\rho}_R^*$ is called the "effective reflectance of the reference cloud."

The effective reflectance of a reference cloud can be obtained as the effective reflectance of bright clouds filling the radiometer's field of view. The emissivity of the clouds giving rise to the reference reflectance may be safely assumed as 1.0, so we write

$$\tilde{\omega}_R^* \cong \tilde{\rho}_R^* , \quad (34)$$

where $\tilde{\omega}_R^*$ is called the "whiteness of the reference cloud."

We now define the "cloudness," C , as a ratio of the whiteness of a cloud to that of a reference cloud, thus

$$C = \tilde{\omega}^* / \tilde{\omega}_R^* . \quad (35)$$

Since the whiteness of a cloud is the ratio of $\tilde{\rho}^*$ and $\tilde{\epsilon}$, it varies according to the direction of the measurement as well as that of the sun. If we assume that the directional variations of reflectance of actual and reference clouds are similar, the cloudness, C , of a specific cloud may be regarded as isotropic. Thus C represents a characteristic of a cloud which does not vary according to the direction of measurement

and that of the sun.

It should be noted, however, that C varies considerably according to the type and thickness of the cloud. As has been discussed earlier, most of the thick convective clouds, such as towering cumuli, thick fog, and stratus, are characterized by $C = 1.0$, according to the definition of the reference cloud. Figure 7 suggests, however, that the cloudness, C , of thin cirrus clouds would be 0.1 - 0.3 for Ci, 0.3 - 0.6 for Cs, and 0.6 - 1.0 for As. Thus the value of C for these clouds varies from nearly 0.0 to nearly 1.0.

6. Equivalent Reference Cloud Cover

The concept of the equivalent whitebody cloud cover, introduced previously and incorporated into Eq. (24), resulted in Eq. (25). If Eq. (25)

$$\bar{A} = n_U \bar{A}_{Uc} + (1 - n_U) \bar{A}_b ,$$

is applied to the case of a thick cloud filling the field of view of the radiometer, it is seen that the equivalent whitebody cloud cover will be less than 1.0 due to the fact that the reflectance of actual bright clouds is around 0.8 or less.

In this case, it is convenient to define an equivalent cloud cover which will result in a value equal to 1.0. After multiplying and dividing Eq. (25) by $\tilde{\rho}_R^*$, the reflectance of the reference cloud, we have

$$\bar{A} = n_R \bar{A}_{Rc} + (1 - n_R \tilde{\rho}_R^*) \bar{A}_b \quad (36)$$

$$\cong n_R \bar{A}_{Rc} + (1 - n_R) \bar{A}_b , \quad (37)$$

where $\bar{A}_{Rc} = \tilde{\rho}_R^* \bar{A}_{Uc}$ and $n_R = n_U / \tilde{\rho}_R^*$.

The quantity \bar{A}_{Rc} is the albedo of a reference cloud replacing the actual cloud and n_R is the equivalent reference cloud cover. The equivalent reference cloud cover represents the cover of a hypothetical reference cloud which reflects the same amount of solar radiation as is reflected by the actual clouds inside the field of view.

The approximation leading to Eq. (37) is accurate with only a few percent of error as long as the satellite-measured albedo of the background is kept less than about 0.2. Thus, this equation is applicable when the background is ocean or ground, except for snow- or sand-covered ground.

The cloudness, C , defined in Eq. (35) as a ratio of whiteness between actual and reference clouds, can be expressed as a function of cloud covers. Equations (33) and (34) now permit us to write

$$C = \frac{\tilde{\omega}_R}{\tilde{\omega}_R^*} = \frac{\tilde{\rho}^*}{\tilde{\epsilon} \tilde{\rho}_R^*} = \frac{1}{n \tilde{\epsilon}} \frac{n \tilde{\rho}^*}{\tilde{\rho}_R^*} = \frac{1}{n_B} \frac{n_U}{\tilde{\rho}_R^*} = \frac{n_R}{n_B} . \quad (38)$$

The albedo of the reference cloud used in Eq. (37) is the product of the reflectance of the reference cloud and the albedo of the white cloud replacing the actual cloud. Using the albedo of the white cloud in Eq. 30, we write the albedo of the reference cloud as

$$\bar{A}_{RC} = \left[1 - k\alpha_0 \frac{\bar{W}_{Bc}}{\bar{W}_{Bb}} \right] \tilde{\rho}_R^* . \quad (39)$$

7. Computation of Effective Radiant Emittance of Clouds and Cloudiness

The equations derived in the previous sections indicate that the radiation values measured by a radiometer with a field of view larger than the areas of the clouds do not represent the effective radiant emittance of the clouds, but represent smeared radiant emittance contaminated by the background radiation. This is also true for thin clouds, even if they fill the entire field of view, because their emissivities and reflectances are small.

In order to determine the effective radiant emittance of a cloud, it must be a black-body and extensive enough to fill the entire field of view. For MRR measurements, occurrences of such conditions will be very rare, because the sensor's half-power scan spots are usually wider than 50 miles. Even with HRIR sensors, both emissivity and cloud coverage could result in serious errors if the measured radiant emittances are assumed to represent those of the clouds. An attempt is therefore made in this section to obtain the effective radiant emittance of clouds from long- and short-wave radiation data for areas of partial cover by various clouds.

In order to combine long- and short-wave measurements, Eq. (15), (37), and the relationship between the effective radiant emittance and the albedo in Eq. (39) are used. Thus we write

$$\bar{W} = n_B \bar{W}_{Bc} + (1 - n_B) \bar{W}_{Bb} , \quad (15)$$

$$\bar{A} \cong n_R \bar{A}_{RC} + (1 - n_R) \bar{A}_b , \quad (37)$$

and

$$\bar{A}_{RC} = \left[1 - k\alpha_0 \frac{\bar{W}_{Bc}}{\bar{W}_{Bb}} \right] \tilde{\rho}_R^* . \quad (39)$$

The eleven quantities appearing in these equations are listed below for clarification.

- \bar{W} , effective radiant emittance measured by a long-wave sensor (known).
- \bar{A} , effective albedo derived from short-wave radiation data (known)
- k , correction factor which may be regarded as 0.6 (constant).
- α_0 , extinction coefficient at sea level computed from the satellite and solar zenith angles (known).
- \bar{W}_{Bb} , effective radiant emittance of the background estimated through a mapping procedure explained later (known).
- \bar{A}_b , effective albedo of the background estimated through a mapping procedure (known).
- $\tilde{\rho}_R^*$, mean reflectance of the reference cloud estimated through a mapping procedure (known).
- \bar{W}_{Bc} , effective radiant emittance of a blackbody replacing an actual cloud (unknown).
- \bar{A}_{Rc} , effective albedo of the reference cloud replacing an actual cloud (unknown).
- n_B , equivalent blackbody cloud cover within the field of view (unknown).
- n_R , equivalent reference cloud cover within the same field of view (unknown).

Thus we have four unknown quantities while only three equations are available. Therefore, one of these unknown quantities can be expressed as a function of seven known quantities plus one unknown quantity which must somehow be estimated.

We shall first obtain the solution of \bar{W}_{Bc} , the effective radiant emittance. Equations (15), (37), and (39) lead to

$$\bar{W}_{Bc} = \frac{\bar{W}_{Bb} - \bar{\pi}C(\tilde{\rho}_R^* - \bar{A}_b)}{\bar{W}_{Bb} - \bar{\pi}Ck\alpha_0\tilde{\rho}_R^*} \bar{W}_{Bb} \quad (40)$$

where

$$\bar{\pi} = (\bar{W}_{Bb} - \bar{W}) / (\bar{A} - \bar{A}_b) \quad (41)$$

is called the "effective pseudo-radiant emittance" and $C = n_R / n_B$ from Eq. (38).

The effective pseudo-radiant emittance introduced here is the reduction of the effective radiant emittance by the clouds inside the field of view divided by the increment of the effective albedo of the same clouds. Therefore, $\bar{\pi}$ is small for low, bright clouds, but large for high, faint clouds. For example, $\bar{\pi}$ will be practically zero for low stratus or thick fog, while it will be extremely large for so-called invisible cirrus

which radiates a certain amount in the spectral range of infrared but reflects very little sunlight.

It will be necessary, at this point, to clarify the physical meaning of the cloudness, C , which is defined in Eq. (38). By definition, C , should be 1.0 if $\tilde{\omega}^*$, the whiteness of the actual cloud, is identical to $\tilde{\omega}_R^*$, the whiteness of the reference clouds which are characterized by the saturation values of $\tilde{\rho}^*/\tilde{\epsilon}$, as shown in Fig. 7. The figure indicates that the whiteness of clouds consisting of cloud droplets of several microns and having several tenths gm^{-3} liquid water content near their tops reaches a saturation value for clouds thicker than about 1 km. Most tall cumuli, cumulonimbi, and thick stratocumuli may therefore be regarded as reference clouds. Even fog, stratus, and small cumuli show over 0.95 cloudness if they consist of small cloud droplets and are several hundred meters thick. In exceptional cases, if clouds have a high concentration of small droplets, such as in the bright tops of rapidly growing cumulus or cumulonimbus clouds, C may reach about 1.10. In general, the cloudness, C , of these clouds may be assumed to be 1.00 with less than 5% error.

Equation (40), when applied to these clouds, can be reduced to

$$\overline{W}_{Bc} = \frac{\overline{W}_{Bb} - \overline{\pi} (\tilde{\rho}_R^* - \overline{A}_b)}{\overline{W}_{Bb} - \overline{\pi} k \alpha_o \tilde{\rho}_R^*} \overline{W}_{Bb} \quad (42)$$

by eliminating $C = 1.00$.

In order to reveal the influence of the cloudness, C , upon the effective radiant emittance of clouds, \overline{W}_{Bc} , computed from Eq. (41), isolines of C ranging between 0.0 and 1.1 were drawn on a \overline{W}_{Bc} vs. $\overline{\pi}$ diagram in Fig. 8, using the values $\overline{W}_{Bb} = 54 \text{ watts m}^{-2}$, $\overline{A}_b = 0.12$, $\tilde{\rho}_R^* = 0.78$, and $\alpha_o = 0.4$. This example shows that the values of \overline{W}_{Bc} computed as a function of $\overline{\pi}$ while assuming that $1.1 > C > 0.9$ fall into a narrow, wedge-shaped domain bounded by two isolines of C . The effective radiant emittance of clouds discussed earlier will be included in this domain when plotted against $\overline{\pi}$, the measured quantity. Thus, we are able to compute \overline{W}_{Bc} from Eq. (42) with a reasonable degree of accuracy.

The next question is how to tell whether or not the cloudness, C , of the clouds inside the field of view is approximately 1.0. To partially answer this question we shall evaluate the values of \overline{W}_{Bc} computed from Eq. (42), which was derived by assuming $C = 1.0$. A restriction is made that \overline{W}_{Bc} must be larger than that of the effective radiant emittance of the coldest cloud tops expected over the region of measurement. Note that \overline{W}_{Bc} from Eq. (42) may result in negative values when $\overline{\pi}$ is extremely large. This means that we cannot compute \overline{W}_{Bc} when $\overline{\pi}$ increases beyond a certain critical

value, which would correspond to the coldest cloud-top temperature expected over the region of measurement. The effective radiant emittance at this temperature is called the "critical effective radiant emittance, $\overline{W}_{\text{CRI}}$ " and the corresponding $\overline{\pi}_{\text{CRI}}$, the "critical pseudo-radiant emittance.

If we assume that the coldest cloud-top temperature, or "critical temperature," T_{CRI} , is that of the local tropopause, we are able to compute $\overline{W}_{\text{CRI}}$ from the estimated tropopause temperature. The effective radiant emittance from extensive and thick high-cloud cover may also be used as a reference. In Fig. 8, it will be shown that the error in estimating $\overline{W}_{\text{CRI}}$ does not appreciably affect the corresponding value of $\overline{\pi}_{\text{CRI}}$ especially when the cloud temperature is very low.

The value $\overline{\pi}_{\text{CRI}}$ is obtained by equating the right side of Eq. (42) with $\overline{W}_{\text{CRI}}$. Thus

$$\overline{\pi}_{\text{CRI}} = \frac{\overline{W}_{\text{Bb}} - \overline{W}_{\text{CRI}}}{\overline{W}_{\text{Bb}}(\tilde{\rho}_{\text{R}}^* - \overline{A}_{\text{b}}) - k\alpha_0\tilde{\rho}_{\text{R}}^*\overline{W}_{\text{CRI}}} \overline{W}_{\text{Bb}} \quad (43)$$

As shown in Fig. 8, $\overline{W}_{\text{CRI}}$ and $\overline{\pi}_{\text{CRI}}$ correspond one-to-one whenever other parameters remain unchanged. If the measured $\overline{\pi}$ is larger than $\overline{\pi}_{\text{CRI}}$ we have to abandon our initial assumption that the value of C of the clouds inside the field of view is approximately 1.0.

Figure 8 indicates the possibility that large values of $\overline{\pi}$ occur when cold clouds are characterized by small values of C . In such a case, C can be computed from Eq. (40) and the estimated value of \overline{W}_{Bc} , so that

$$C = \frac{\overline{W}_{\text{Bb}} - \overline{W}_{\text{Bc}}}{\overline{W}_{\text{Bb}}(\tilde{\rho}_{\text{R}}^* - \overline{A}_{\text{b}}) - k\alpha_0\overline{W}_{\text{Bc}}\tilde{\rho}_{\text{R}}^*} \frac{\overline{W}_{\text{Bb}}}{\overline{\pi}} = \frac{\overline{\pi}_{\text{R}}}{\overline{\pi}} \quad (44)$$

where

$$\overline{\pi}_{\text{R}} = \frac{\overline{W}_{\text{Bb}} - \overline{W}_{\text{Bc}}}{\overline{W}_{\text{Bb}}(\tilde{\rho}_{\text{R}}^* - \overline{A}_{\text{b}}) - k\alpha_0\overline{W}_{\text{Bc}}\tilde{\rho}_{\text{R}}^*} \overline{W}_{\text{Bb}} \quad (45)$$

denotes the effective pseudo-radiant emittance of a reference cloud replacing the actual cloud. Using these equations, we can compute the cloudness, C , of a cloud whose temperatures can be estimated.

8. Computation of Equivalent Blackbody, Equivalent Reference, and Photographic Cloud Covers

As has been discussed in the previous section, the cloudness, C , of clouds inside the field of view is assumed to be 1.0 when $\overline{\pi}$ is less than $\overline{\pi}_{\text{CRI}}$. In reality, however, this assumption is not valid when thin, middle clouds as indicated in Fig. 8 are involved, although such a case seems to be the exception. Under the assumption that $C = 1.0$, we compute \overline{W}_{Bc} from Eq. (42) and solve Eq. (15) to obtain

$$n_B = \frac{\bar{W}_{Bb} - \bar{W}}{\bar{W}_{Bb} - (\bar{W}_{Bc})_{\text{comp.}}} , \quad (46)$$

where $(\bar{W}_{Bc})_{\text{comp.}}$ refers to a computed value.

Further,

$$n_R = n_B \quad (47)$$

according to Eq. (38).

When the computed $\bar{\pi}$ is larger than $\bar{\pi}_{\text{CRI}}$, we have to estimate \bar{W}_{Bc} in order to compute C from Eq. (44). Since extremely large values of $\bar{\pi}$ occur with thin, high clouds, \bar{W}_{Bc} can be estimated with reasonable accuracy. Note that a 10 C error in estimating cirrus temperature does not alter \bar{W}_{Bc} appreciably. We are thus able to compute reasonable values of C and $\bar{\pi}_R$ from Eq. (44) and (45). From the estimated value of \bar{W}_{Bc} and the computed value of C, we obtain

$$n_B = \frac{\bar{W}_{Bb} - \bar{W}}{\bar{W}_{Bb} - (\bar{W}_{Bc})_{\text{est.}}} , \quad (48)$$

where $(\bar{W}_{Bc})_{\text{est.}}$ refers to an estimated value,

$$\text{and} \quad n_R = n_B(C)_{\text{comp.}} . \quad (49)$$

We shall now discuss the feasibility of computing the radiometric cloud cover by using a satellite photograph taken simultaneously with the radiation measurement. Remembering that we are using a two-radiance model involving unique radiances for clouds and background inside the field of view, we rewrite Eq. (9) in the form

$$n = \frac{\int \phi_{\Omega} d\Omega_c}{\int \phi_{\Omega} d\Omega} = \frac{\int d\beta_c}{\int d\beta} , \quad (50)$$

where $d\beta = \phi_{\Omega} d\Omega$. Then we divide $\int d\beta$ into an equal value of $\Delta\beta$ satisfying

$$\Delta\beta = \frac{1}{m} \int d\beta .$$

Thus, $\Delta\beta$ represents the fractional sensitivity of a radiometer. When the entire field of view is divided into m parts of identical fractional sensitivity, $\Delta\beta$, only m_c parts will be covered with clouds of identical radiance when the field of view is partially cloud covered. We may, therefore, reduce Eq. (50) to

$$n_p = \frac{m_c \Delta\beta}{m \Delta\beta} = \frac{m_c}{m} , \quad (51)$$

which is the radiometric cloud cover obtained from a satellite photograph by counting the number of cloud-covered parts, m_c , after dividing the radiometer's field of view into m parts of identical fractional sensitivity, $\Delta\beta$. This cloud cover, n_p , is called the "photographic cloud cover."

Experience shows that m should be at least 10 in order to estimate n with a 10% or better accuracy. Figure 9 is an example in which $m = 100$ was used. Since we are assuming a two-radiance model which allows only one radiance for clouds inside the field of view, it is necessary to make a "yes" or "no" type of decision when the number m_c is determined. For clouds with sharp boundaries, there will not be any problem in determining the number even if the photographs are printed too dark or too light. Depending upon the dynamical range of photo representation, the radiometric cloud cover computed from a photograph will, however, vary to a certain extent.

It should be noted that the photographic cloud cover is usually larger than the reference cloud cover because the latter represents the cloud cover by the reference clouds replacing the actual clouds without changing the total radiation within the field of view.

9. Computation of Cloud Emissivity and Cloud Reflectance

The equivalent blackbody cloud cover introduced by reducing Eq. (13) into (15) is written as

$$n_B = n\tilde{\epsilon}$$

By using this relationship together with the photographic cloud cover obtained from a photograph, we obtain the emissivity of clouds as

$$\tilde{\epsilon} = n_B/n_p, \quad (52)$$

where n_B is computed from either Eq. (46) or (48).

The equivalent reference cloud cover defined by

$$n_R = n_U/\tilde{\rho}_R^* \quad \text{and} \quad n_U = \tilde{\rho}^* n$$

can, according to Eqs. (25) and (37), be combined into

$$n_R = n \frac{\tilde{\rho}^*}{\tilde{\rho}_R^*}$$

which permits us to compute the reflectance of the clouds, $\tilde{\rho}^*$, as

$$\tilde{\rho}^* = \frac{n_R}{n_p} \tilde{\rho}_R^*$$

or

$$\tilde{\rho}^* = \tilde{\epsilon} C \tilde{\rho}_R^*, \quad (53)$$

since all quantities on the right side are already known.

The reflectance of clouds from this equation differs from the albedo, which includes atmospheric attenuation.

10. Mapping Procedures for Estimating \bar{A}_b , $\tilde{\rho}_R^*$, and \bar{W}_{Bb}

For input to Eq. (15), (37), and (39) listed in Section 7, we have to estimate three quantities; \bar{W}_{Bb} , the effective radiance of the background; \bar{A}_b , the effective albedo of the background; and $\tilde{\rho}_R^*$, the reflectance of the reference cloud in the direction of the satellite.

First, we select on a satellite picture large cloud-free areas which may be regarded as $n=0$. For these areas both n_b and n_R should also be zero by definition. The measured values of \bar{W} and \bar{A} from these areas are written simply as

$$\bar{W} = \bar{W}_{Bb} \quad \text{and} \quad \bar{A} = \bar{A}_b \quad (54)$$

From these relationships we compute \bar{W}_{Bb} and \bar{A}_b from all cloud-free areas and plot them on two separate maps as shown in Fig. 10. Then, we draw isolines of these values, keeping in mind the fact that the finite field of view of a radiometer results in smoothed patterns of \bar{W}_{Bb} and \bar{A}_b , even though they change abruptly along coast lines or in high mountain areas. If plotted values show certain variations within a small area, we should put less weight on higher albedo and lower radiant emittance, which are likely to be caused by the existence of unnoticeable clouds inside the field of view and/or clouds in the outermost portion of the scan spot. It should be noted that the solid angle of a 100%-power scan spot of a MRIR is about 9 times larger than that of a 50%-power scan spot. If we try to select areas without clouds within a 100%-power scan spot, it is very unlikely that we will find any.

Thus, after completing smooth isolines for \bar{W}_{Bb} and \bar{A}_b , we are able to interpolate these values as a function of longitude and latitude anywhere within the area of analysis.

The extinction coefficient, α_0 , such as shown in Fig. 3, can be computed from both satellite and solar zenith angles given for each scan spot. The values in Fig. 10 were obtained from these angles by using isolines for α_0 appearing in Fig. 3.

The mapping of $\tilde{\rho}_R^*$, the reflectance of the reference cloud, can be made by selecting extensive areas of bright clouds likely to represent the characteristics of reference clouds. If such clouds cover the entire field of view, we may consider that $n = n_b = n_R = 1.0$, thus permitting us to reduce Eq. (15), (37), and (39) to

$$\bar{A} = \left[1 - k\alpha_0 \frac{\bar{W}}{\bar{W}_{Bb}} \right] \tilde{\rho}_R^* ,$$

which can be written as

$$\tilde{\rho}_R^* = \bar{A} \left[1 - k\alpha_0 \frac{\bar{W}}{\bar{W}_{Bb}} \right]^{-1} \quad (55)$$

This equation shows that $\tilde{\rho}_R^*$ can be computed from the measured values of \bar{A} and \bar{W} and the estimated values of α_0 and \bar{W}_{Bb} while assuming $k = 0.6$. After plotting $\tilde{\rho}_R^*$ on a map as shown in Fig. 10, we draw the isolines, keeping in mind that the reflectance varies considerably with the scattering angles as determined by the orbital and scan geometry. An example in the figure reveals anisotropic variation of the reflectance.

After completing these mapping procedures, we obtain as a function of scan spot the estimated values of \bar{W}_{Bb} , \bar{A}_b , and $\tilde{\rho}_R^*$, which are put into Eqs. (42) and (44) for computation of \bar{W}_{Bc} , the effective radiant emittance of clouds and C , the cloudness.

11. Effects of Sensor Degradation on Computations of Cloud Parameters

We have, so far, developed equations and procedures while assuming that satellite-measured quantities are not influenced by sensor degradation. It is safe, however, to assume that these quantities include a certain error resulting from uncorrected degradation even after initial attempts for degradation correction have been made.

Under the assumption that the true values and the measured values are related by

$$\bar{A} = g\bar{A}$$

and
$$\bar{W} = h\bar{W} \quad , \quad (56)$$

where "=" represents the measured value and "-", the true value. Both g and h will be 1.0 if the entire degradation has been corrected previously.

Since we estimate $\tilde{\rho}_R^*$ through the mapping procedure using Eq. (55), the effects of uncorrected degradation on the estimated value will be known by putting Eq. (56) into Eq. (55) so that

$$\begin{aligned} \tilde{\rho}_R^* &= g\bar{A} \left[1 - k\alpha_0 \frac{\bar{W}}{\bar{W}_{Bb}} \right]^{-1} \\ &\equiv g\tilde{\rho}_R^* \quad , \end{aligned} \quad (57)$$

where $\tilde{\rho}_R^*$ denotes the reflectance computed from Eq. (55) using measured values which include linear degradation as defined in Eq. (56).

Now we replace the true measured values in Eq. (15), (37), and (39) with the degraded measured values in Eq. (56) and (57) to write

$$\bar{W} = n_B \bar{W}_{Bc} + (1 - n_B) \bar{W}_{Bb} \quad ,$$

$$\bar{A} = n_R \bar{A}_{Rc} + (1 - n_R) \bar{A}_b \quad ,$$

and

$$\bar{A}_{Rc} = \left[1 - k\alpha_o \frac{\bar{W}_{Bc}}{\bar{W}_{Bb}} \right] \tilde{\rho}_R^* \quad , \quad (58)$$

which reveals that this set of equations keeps the same form when degraded values are used instead of true values. This means that all solutions obtained by using true values can immediately be altered into those including degraded values.

The effective pseudo-radiant emittance, $\bar{\pi}$, can thus be expressed as

$$\bar{\pi} = \frac{\bar{W}_{Bb} - \bar{W}}{\bar{A} - \bar{A}_b} = \frac{h}{g} \frac{\bar{W}_{Bb} - \bar{W}}{\bar{A} - \bar{A}_b} = \frac{h}{g} \bar{\pi} \quad , \quad (59)$$

where $\bar{\pi}$ denotes the effective pseudo-radiant emittance computed from degraded values.

The effective radiant emittance, \bar{W}_{Bc} , from Eq. (42) can be written as

$$\bar{W}_{Bc} = h \frac{\bar{W}_{Bb} - \bar{\pi} (\tilde{\rho}_R^* - \bar{A}_b)}{\bar{W}_{Bc} - \bar{\pi} k\alpha_o \tilde{\rho}_R^*} \bar{W}_{Bb} = h \bar{W}_{Bc} \quad , \quad (60)$$

where \bar{W}_{Bc} is the value computed from degraded values. It is important that \bar{W}_{Bc} is not affected by the linear degradation of the short-wave sensor; thus only the correction of degradation for the long-wave sensor is required.

It is of interest that C , the cloudiness from Eq. (44),

$$C = \bar{\pi}_R / \bar{\pi} = \bar{\pi}_R / \bar{\pi} \quad , \quad (61)$$

is not affected by degradation of either the long or the short-wave sensor. Likewise, the equivalent blackbody cloud cover, n_B , and the equivalent reference cloud cover from Eq. (46) and (47) are not affected by these degradations.

Finally, we shall discuss errors in the emissivity, $\tilde{\epsilon}$, and the reflectance of clouds. From Eq. (52), we write

$$\tilde{\epsilon} = \frac{n_B}{i \bar{n}_p} = \frac{1}{i} \tilde{\epsilon} \quad , \quad (62)$$

where $i = n_p / \bar{n}_p$ is the linear error in estimating the photographic cloud cover. It is evident that overestimation of the cloud cover ($i < 1.0$) reduces the emissivity. The reflectance of clouds, $\tilde{\rho}^*$, as expressed by Eq. (53) is affected by both g and i ; thus

$$\tilde{\rho}^* = \frac{1}{i} \tilde{\epsilon} C g \tilde{\rho}_R^* = \frac{g}{i} \tilde{\epsilon} C \tilde{\rho}_R^* = \frac{g}{i} \tilde{\rho}^* \quad , \quad (63)$$

where $\tilde{\rho}^*$ is the cloud reflectance computed by using degraded short-wave data and the improper radiometric cloud cover.

Table II summarizes the influence of degradation and error in the estimation of radiometric cloud cover.

Table II. Summarized effects of correction factors, g for short-wave degradation, h for long wave degradation, and i for radiometric cloud cover. Yes means "affected."

Correction factors	g	h	i
\bar{W}_{Bc} , eff. rad. emit. of clouds	NO	YES	NO
C, the cloudness	NO	NO	NO
n_B , equiv. blackbody cloud cover	NO	NO	NO
n_R , equiv. reference cloud cover	NO	NO	NO
$\tilde{\epsilon}$, cloud emissivity	NO	NO	YES
$\tilde{\rho}^*$, cloud reflectance	YES	NO	YES

12. Application to the Meteorological Interpretation of Radiation Data

The preceding sections have clarified that the measured values of effective radiant emittance and effective reflectance are quite different from those of clouds themselves, mainly because a scan spot includes both clouds and their background. The High Resolution Infrared Radiometer (HRIR) on board Nimbus I had a field of view almost two orders of magnitude smaller than that of the TIROS Medium Resolution Radiometers (MRR). In their study of the Nimbus HRIR, Fujita and Bandeen (1965) demonstrated that most of the noise can be eliminated by taking one-degree running means of analog signals recorded on the master telemetry tapes. A one-degree rotation of the radiometer axis would displace the scan point as much as 10 km when scanning from a 500-km altitude, elongating a circular, half-power scan spot into an elliptic spot about 5-km wide and 10-km long in the direction of scan.

We expect that HRIR scan spots are filled with uniform effective radiant emittance more often than those of MRR. Nevertheless, the chances of measuring smeared cloud and background radiant emittances must not be underestimated because the spot is still too large to expect uniformly distributed radiant emittance within the spot of radiation measurement. Another serious problem is the influence of emissivity on the determination of cloud-top temperature. The reduction of the field of view beyond a certain

limit, therefore, does not always improve the accuracy of temperature measurement. The basic problems discussed in this paper based on MRR data will, therefore, remain practically the same in the case of HRIR and super-HRIR data, when these data exist.

MRR Mapping Directly from Analog Traces

In order to calculate various parameters by using equations presented in this paper, it is necessary to assume that a scan spot is filled with two effective radiant emittances designating clouds and background, respectively. When the scan-spot area is very small, this requirement will be met.

Grid-point maps are convenient forms of large-scale radiation pattern presentation. As shown in the Radiation Data Catalog of TIROS III, NASA (1962), 1:5,000,000 maps give relatively unsmoothed patterns, but the small-scale maps are produced after averaging the data inside each 2.5° square of geocentric angle. The number of data points inside a given square, which is called the "population", could be 50 or even larger near the inner scan boundary. In most cases, the smoothed values thus obtained cannot be used for investigation of mesoscale disturbances and background.

An analog trace recorded directly from the master telemetry tapes retains detailed meteorological variations before smoothing through grid-point mapping processes. Presented in Fig. 11 are an oscillograph analog trace and a Brush Recording Instrument analog trace. The former includes every variation as recorded on the telemetry tape, but the latter gives slightly smoothed variations. The Final Meteorological Radiation Tape (FMRT) is produced by sampling data for every 72nd or 36th cycle of the satellite clock (550 cps), thus including 7.64 or 15.28 data points per second of sampling time. The numbers of sampling points from one perinadir to the next are about six times the above numbers, because a TIROS spins at about 10 revolutions per minute. It may be assumed that FMRT listing includes the above numbers of points read out from the oscillograph trace at constant time intervals. The data from FMRT are not smoothed as are the grid print maps, permitting us to use them for computing various parameters presented in this paper.

Since the "Scanning Printer" designed by Fujita (1964) is available at the University of Chicago, all maps presented in this paper were done on the printer, which produces a sigma-t printout while a brush analog trace is followed by the operator of the machine. An example of radiation maps thus obtained is presented in Fig. 12, which shows the isotherms of T_{BB} converted from \bar{W} measured over the region of Hurricane Anna on July 21, 1961, TIROS III, Orbit 132, R/O 133 between 1546 and 1549 GMT. The pattern of isotherms shows $-73C$ to be the coldest temperature, probably corresponding to the

top of active penetrative towers forming a rainband. A scan line extending from 10N, 76W to 17N, 72 W in the figure passes near the center of the storm where a small warm area identified as "W" is seen in the map. This is probably the eye of Anna. The analog traces in Fig. 11, in fact, represent the radiation from this particular scan; thus, the time variations in the traces correspond to the space variations of T_{BB} along the scan line. The scan angles in degrees are entered for the purpose of matching the traces and the map.

The map is divided into 12 sections by geographic grid lines drawn at 2.5° intervals. If this map were converted into a small-scale grid print map, the average value from each section would be obtained by a computer, and then isolines could be drawn. It is concluded, therefore, that this kind of map or FMRT listings can be used in testing the validity of equations derived in this paper.

Jet-Stream Cirrus and an Anvil Cloud over Italy

The equivalent blackbody temperatures mapped over Hurricane Anna seem to fit the cloud-top temperatures fairly well because a rather extensive cirrus shield covering the storm top is viewed. When jet-stream cirrus clouds are mapped using the same technique, however, it is found that some faint cirrus does not appear to be as cold as it should be.

Figure 13 shows an example of T_{BB} isotherms drawn on a TIROS IV picture taken over the Mediterranean on Feb. 15, 1962. The coastlines of Italy and northern Africa will identify the photographic coverage. The lowest T_{BB} , $-43C$, is seen over Central Italy where thunderstorms are in progress. A detailed description of this situation appears in a paper by Rabbe and Fujita (1964).

The patterns of T_{BB} fit almost precisely to the cloud picture, so that the temperature of each cloud mass can be read off from isotherms drawn for every $2C$.

In order to find the validity of T_{BB} mapped over the jet-stream region, the pseudo-radiant emittance $\bar{\pi}$ was first computed. When the cirrus temperature is assumed to be $-39C$, which is $4C$ warmer than the coldest cumulonimbus top over Italy, a stippled area in Fig. 14 is characterized by $\bar{\pi}$ which is larger than $\bar{\pi}_{CRI}$ corresponding to the cirrus temperature. The cloudiness, C , was thus computed inside this area by using Eq. 44. It is important to note that the area of small C extends downwind from the top of convective storms reaching jet-stream levels. The smallest cloudiness, 0.6 or less, is seen near the lower-right picture corner.

For further investigation of the cloudiness and other parameters, an anvil cloud extending downwind from a mass of thunderstorms in Italy was selected. A rectified

cloud pattern depicted with two gray-scale contours is shown in Fig. 15. Fortunately, scan lines 91 through 96 crossed the long anvil at nearly right angles resulting in more distinct variation than in the cases of crossing with other angles. As shown in the figure the scan spot of 50% power was 60 X 80 km, and that of 80% power was as large as 100 X 150 km, so that the measured radiation values definitely included both cloud and background radiation.

Shown also in Fig. 15 are the analog traces of Channels 2 and 3 which were used in calculating various parameters presented in Table III, in which the computation points A through H are located at the intersections of the anvil axis and the scan lines. Various parameters used in computing this table are $T_{Bc} = -39^{\circ}\text{C}$, $\bar{W}_{Bc} = 14.8 \text{ watts m}^{-2}$, $\bar{W}_{Bb} = 34.0 \text{ watts m}^{-2}$, and $\bar{A}_b = 0.02$, which were estimated from measured values.

Table III. Computed effective pseudo-radiant emittance, equivalent blackbody and reference cloud covers, cloudness, and emissivity of an anvil cloud extending from a thunderstorm over central Italy, Feb. 15, 1962. Photographic and radiation data are from TIROS IV, Orbit 99.

Computation points	A	B	C	D	E	F	G	H
\bar{W} in watts m^{-2}	14.8	17.0	22.0	27.0	28.5	30.0	28.0	28.5
\bar{A}	0.55	0.41	0.26	0.15	0.11	0.10	0.09	0.10
Anvil width in km	60	30	40	60	70	60
$\bar{W}_b - \bar{W}$ in watts m^{-2}	19.2	17.0	12.0	7.0	7.0	5.5	4.0	5.5
$\bar{A} - \bar{A}_b$	0.53	0.39	0.24	0.13	0.09	0.08	0.07	0.08
$\bar{\pi}$ in watts m^{-2}	36	44	50	54	61	50	85	69
$C = \bar{\pi}_R / \bar{\pi}$	1.00	0.82	0.72	0.67	0.59	0.72	0.42	0.52
$n_B = \bar{W}_{Bb} - \bar{W} / \bar{W}_{Bb} - \bar{W}_{Bc}$	1.00	0.88	0.62	0.36	0.28	0.21	0.31	0.28
$n_R = C n_B$	1.00	0.72	0.45	0.24	0.17	0.15	0.13	0.15
n_p from picture	1.00	0.90	0.75	0.55	0.50	0.50	0.60	0.55
$\tilde{\epsilon} = n_B / n_p$	1.00	0.98	0.82	0.65	0.56	0.42	0.51	0.39
T_{BB} in $^{\circ}\text{C}$	-39	-33	-21	-12	-9	-6	-10	-9
T_{Bc} in $^{\circ}\text{C}$	-39	-39	-39	-39	-39	-39	-39	-39
$T_{BB} - T_{Bc}$ in $^{\circ}\text{C}$	0	+6	+18	+27	+30	+33	+29	+30

The result of computation will be seen in graphs given in Fig. 16. The top chart reveals the change in the measured values of \bar{W} and \bar{A} . Three cloud covers, photographic, equivalent blackbody, and equivalent reference, decrease almost equally as the distance from the source increases. It should be pointed out that the photographic cloud cover underwent the least change, probably because of the diffusion of ice crystals which tends to increase the areal coverage. A decrease in the equivalent blackbody and equivalent reference cloud covers may be caused by sublimation which dissipates small ice crystals when the ambient atmosphere is not saturated with respect to ice crystals. If the atmosphere is supersaturated, n_B will probably increase due to the growth of ice crystals.

Emissivity and cloudness of the anvil decreased almost exponentially as the distance from the major thunderstorms increased. This variation of emissivity suggests that the anvil quickly loses its blackbody characteristics. The cloudness, on the other hand, is related to both the density and the size of the ice crystals forming an anvil. The fact that large ice crystals are less reflective than small ones might indicate that the tail end of the anvil lost most of the small crystals, leaving only large ones which survived through the 300-km journey downwind.

As a result of small values of the equivalent blackbody cloud cover, which includes both emissivity and photographic cloud cover, the equivalent blackbody temperature of cirriform clouds is sometimes much higher than actual cloud-top temperature. The temperature difference $T_{BB} - T_{Bc}$ denotes the difference between the true cloud-top temperature and the equivalent blackbody temperature measured when a sensor points toward the cloud. Large differences over 30C are seen inside the regions of cirriform clouds. Moderate to large differences appear elsewhere, because a small equivalent blackbody cloud cover always increases the measured T_{BB} considerably (Fig. 14).

Equivalent Blackbody and Equivalent Reference Cloud Covers

In order to determine the difference between the infrared and the visual cloud covers, the authors' method of computing equivalent blackbody and equivalent reference cloud covers was applied to the July 12, 1961, case studied by Fritz, Krishna Rao, and Weinstein (1964) and Maykut (1964). The area covers the East-Central United States where abundant supporting synoptic data are available.

Figure 17 shows a gridded picture covering a portion of the area studied by the aforementioned authors. It is seen that a large overcast area dominates the southern half of the picture, while faint cirriform clouds extend from Indiana to Pennsylvania, resulting in a favorable situation for cloud cover studies.

The contour lines of equivalent blackbody cloud cover presented in Fig. 18 reveal that the stippled area indicating more than 50% cloud cover extends to Lake Erie beyond the northern limit of 50% cloud cover estimated from the satellite photograph. Analysis of reflected solar radiation made by the aforementioned authors also shows that the measured reflectance drops sharply along the northern edge of the overcast region.

The pattern of equivalent reference cloud cover presented in Fig. 19 corresponds rather well with the areas of clouds seen in the satellite picture. The equivalent reference cloud cover over western Lake Erie, for instance, increases almost three times when converted into equivalent blackbody cloud cover, revealing the fact that the cloud cover increases considerably when measured with an infrared sensor. Another example appears over the Pennsylvania-Ohio border, where there was a hole of practically zero equivalent reference cloud cover. When measured by the Channel 2 sensor, its equivalent blackbody cloud cover turned out to be more than 0.3. So-called invisible cirrus could be found in such areas where the cloud cover can be measured with a long-wave but not with a short-wave sensor.

Equivalent Reference Cloud Cover and Photographic Cloud Cover

In an attempt to find to what extent clouds with sharp boundaries are regarded as reference clouds, both photographic and equivalent reference cloud covers were computed independently. Figure 20 shows the computed values of equivalent reference cloud covers (%) plotted on a satellite picture from TIROS IV, orbit 99, shown previously in Fig. 13. Significant spots, such as bright or dark areas, were selected as data points in computing cloud covers; then, the cloud covers were contoured for every 5% increment of equivalent reference cloud cover.

Independent of these cloud covers, the photographic cloud covers were computed from Eq. (51) using the same spots on the photograph. The position designating each cloud was plotted on the n_R vs n_p coordinates in Fig. 21. In obtaining this scatter diagram, each computation spot including non-cirrifiform clouds, as judged on the picture, is shown as a black circle, while others are shown as open circles. The result indicated that the two cloud covers are more or less the same if we exclude the spots including cirrifiform clouds and that the equivalent reference cloud cover of cirrifiform clouds is considerably smaller than the photographic cloud cover, strongly suggesting that cirrifiform clouds are rather unlike the reference clouds.

This evidence supports an assumption in Section 7 that C , the cloudness of non-cirrifiform clouds, may be regarded as 1.0 while that of cirrifiform clouds shows a wide range

of variation, ranging between 0.0 to 1.0.

13. Conclusions

A solution of the radiometer power equation, including both spectral and spatial responses, was obtained in such a form that the influence of clouds and their background inside a scan spot can be separated by combining short- and long-wave radiation data obtained by scanning radiometers. It is feasible to compute cloud covers inside a scan spot despite the fact that the cloud distribution within it remains unknown. Three cloud covers are defined in this paper: n_R , the equivalent reference cloud cover; n_B , the equivalent blackbody cloud cover; and n_p , the photographic cloud cover. The first and second covers can be obtained from long- and short-wave radiation data, but the third cover depends upon how the boundaries of the actual clouds are defined and can be estimated from a satellite picture showing well-defined cloud boundaries. The first cloud cover divided by the second and the second divided by the third represent cloudiness and emissivity, respectively. A test analysis of a long anvil cloud about 50-km wide revealed that TIROS MRR data are sufficiently accurate to determine these parameters and to permit a physical interpretation of radiation data.

While the emissivity computed from MRR data involves important blackbody characteristics of clouds, their cloudiness, which can also be computed from the same data, implies that it is closely related to the size of the ice crystals that form high clouds. It is expected that future studies of these parameters will pave the way for an understanding of so-called invisible cirrus.

An analysis of errors in the computed parameters resulting from errors in the measured quantities was presented in Table II. It is seen that the computed values of C , the cloudiness; n_B , the equivalent blackbody cloud cover; and n_R , the equivalent reference cloud cover are not affected by errors in the measured quantities and, therefore, can be computed without correcting for the degradation of the sensors. On the other hand, the computed values of \bar{W}_{Bc} , the effective radiant emittance of cloud; $\tilde{\epsilon}$, the emissivity of cloud, and $\tilde{\rho}$, reflectance of cloud are affected by one or two of the errors in measurements by the short- and long-wave sensors and of the photographic cloud cover.

It should be noted that \bar{W}_{Bc} , computed from Eq. (42) with long-wave sensor degradation added, represents the effective radiant emittance of a blackbody placed at the top of the clouds. If the correction for atmospheric absorption is known, \bar{W}_{Bc} can be converted into T_{Bc} , the equivalent blackbody temperature of the cloud top. Thus, the

equivalent blackbody temperature can be used to determine the height of the cloud top when the vertical distribution of ambient temperature can be estimated.

Acknowledgements: The authors are grateful to Drs. Sigmund Fritz of ESSA and William Nordberg of NASA for their valuable comments during the course of development of this research. Sincere appreciation is also expressed to Messrs. Linwood Whitney, Jr., of ESSA and William Bandeen of NASA for their assistance in completing the research reported in this paper.

REFERENCES

- Brewer A. W., and J. T. Houghton, 1956: Some measurements of the flux of infrared radiation in the atmosphere. Proc. Roy. Soc. London. Series A, 236, 175-186.
- Bullrich, K., 1948: Lichtdurchlässigkeit in Wolken. Z. Meteor., 2, 321-325.
- Elterman, L., 1964: Parameters for attenuation in the atmospheric windows for fifteen wavelengths. Applied Optics, 3, 1139-1146.
- Fritz, S., 1950: Measurements of the albedo of clouds. Bull. Amer. Meteor. Soc., 31, 25-27.
- _____, 1954: Scattering of solar energy by clouds of "large drops." J. of Met., 11, 291-300.
- _____, P. Krishna Rao, and M. Weinstein, 1964: Satellite measurements of reflected solar energy and the energy received at the ground. J. Atmos. Sci., 21, 141-151.
- Fujita, T., 1964: The scanning printer and its application to detailed analysis of satellite radiation data. SMRP Research Paper No. 34, University of Chicago.
- _____, and W. Bandeen, 1965: Resolution of the Nimbus high resolution infrared radiometer. J. Appl. Met., 4, 492-503.
- Gates, D. M. and C. C. Shaw, 1960: Infrared transmission of clouds. J. Optical Soc., 50, 876-882.
- Handbook of Geophysics, 1961: Geophysics research directorate, Fig. 16-10.
- Kikuti, Y., M. Yamazaki, T. Okawa, and Y. Morita, 1954: Transmission of solar radiation through fog. The Geoph. Mag., Tokyo, 26, 83-92.
- Kuhn, P. M., 1963: Measured effective long-wave emissivity of clouds. Mon. Wea. Rev., 91, 635-640.
- Maykut, E. S., 1964: An experiment in objective nephanalysis using proposed HRIR satellite infrared radiation data. J. Appl. Met., 3, 215-225.
- McDonald, J. E., 1960: Absorption of atmospheric radiation by water films and water clouds. J. of Met. 17, 232-238.
- NASA, 1961, 1961, 1963, and 1964: TIROS II, III, IV, and VII Radiation Data Users' Manuals. Goddard Space Flight Center, Greenbelt, Md.
- NASA, 1962: TIROS III Radiation Data Catalog. Goddard Space Flight Center, Greenbelt, Md.
- Neiburger, M., 1949: Reflection, absorption, and transmission of insolation by stratus cloud. J. of Met., 6, 98-104.

- Nordberg, W., W.R. Bandeen, B.J. Conrath, V. Kunde, and I. Persano, 1962: Preliminary results of radiation measurements from the TIROS III meteorological satellite. J. Atmos. Sci., 19, 20-29.
- Rabbe, A. and T. Fujita, 1964: Synoptic study of cold air outbreak over the Mediterranean using satellite photographs and radiation data. SMRP Research Paper No. 35, University of Chicago.
- Rasool, S.I., 1964: Cloud heights and nighttime cloud cover from TIROS radiation data. J. Atmos. Sci., 21, 152-156.
- Smithsonian Meteorological Tables, 1958: Sixth Rev. Ed., prepared by Robert J. List.
- Wark, D.Q., G. Yamamoto, and J.H. Lienesch, 1962: Methods of estimating infrared flux and surface temperature from meteorological satellites. J. Atmos. Sci., 19, 369-384.
- Wexler, Raymond, 1964: Infrared and visual radiation measurements from TIROS III. Appl. Optics, 3, 215-219.
- Whitney, L.F., Jr., 1965: Jet streams. Proceedings of the Inter-Regional Seminar on the Interpretation and Use of Meteorological Satellite Data, Japan Meteorological Agency, Tokyo, 121-137.

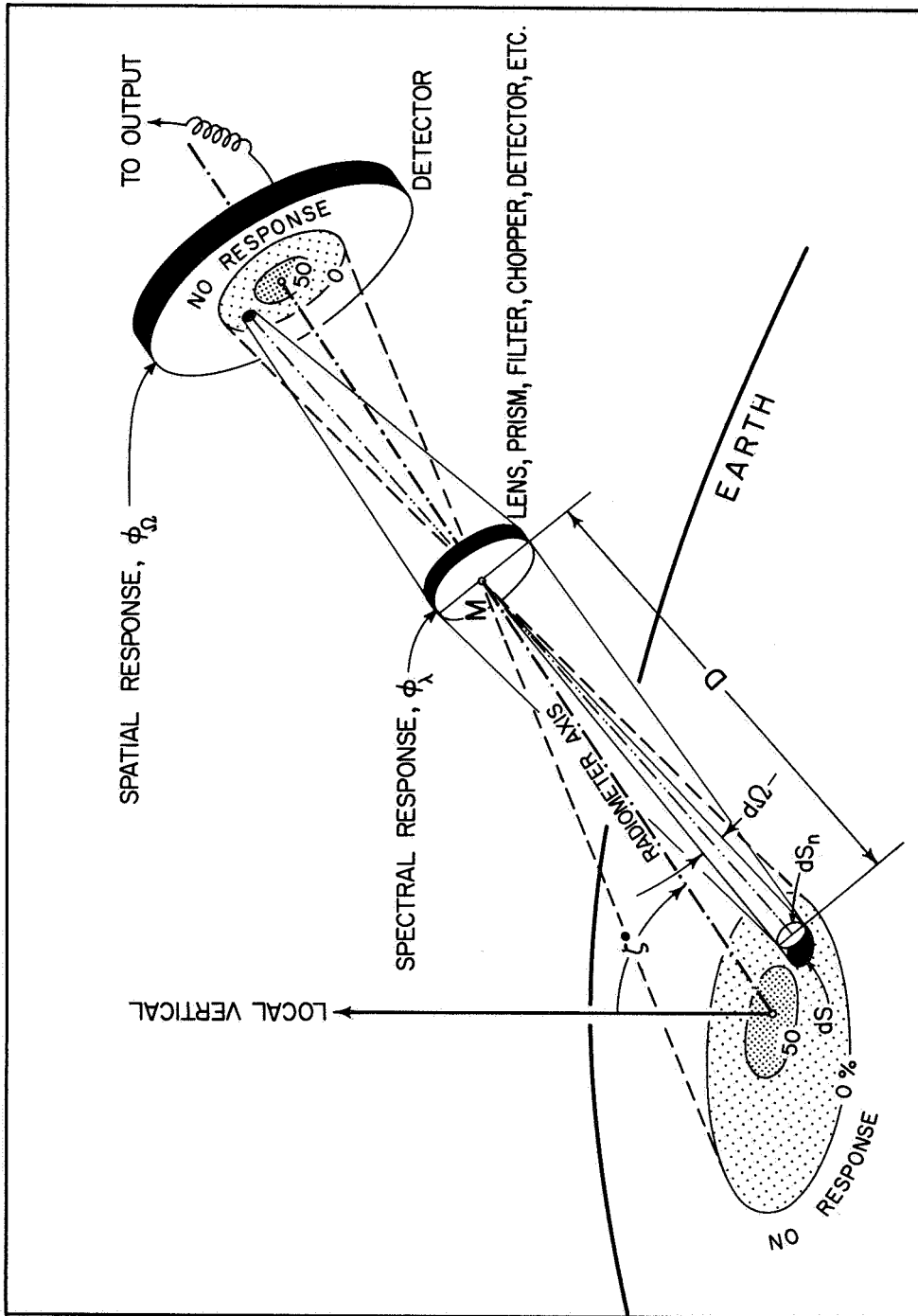


Fig. 1. Schematic diagram showing the spectral and spatial responses of a scanning radiometer. Symbols are: ζ , satellite zenith angle; dS , and area element inside a scan spot; dS_n , normal component of dS ; and $d\Omega$, solid angle of the area element viewed from the satellite. It is seen that the effective radiant emittance measured by a radiometer is restricted by both spectral and spatial responses.

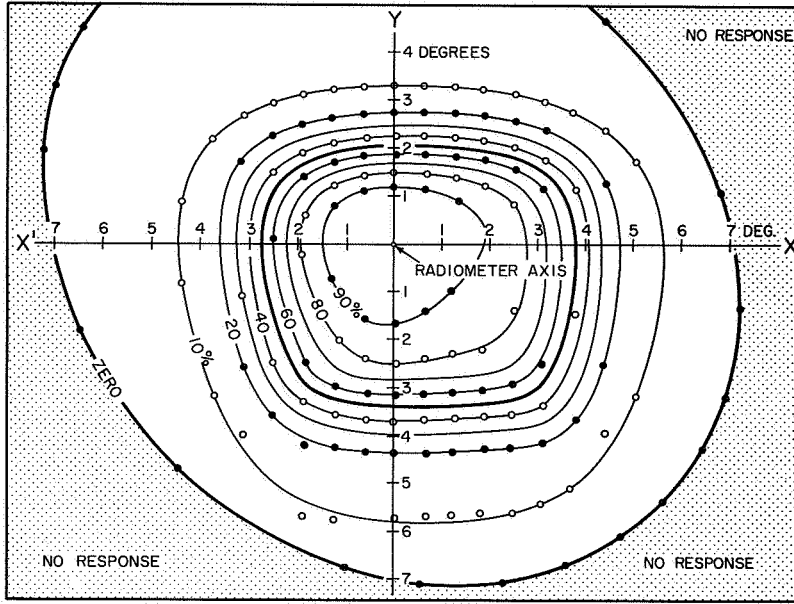


Fig. 2. Solid-angular distribution of the spatial response inside the field of view of a Channel 2 sensor. Note that the response is not axially symmetric and that zero-response boundary extends more than 7° in certain directions.

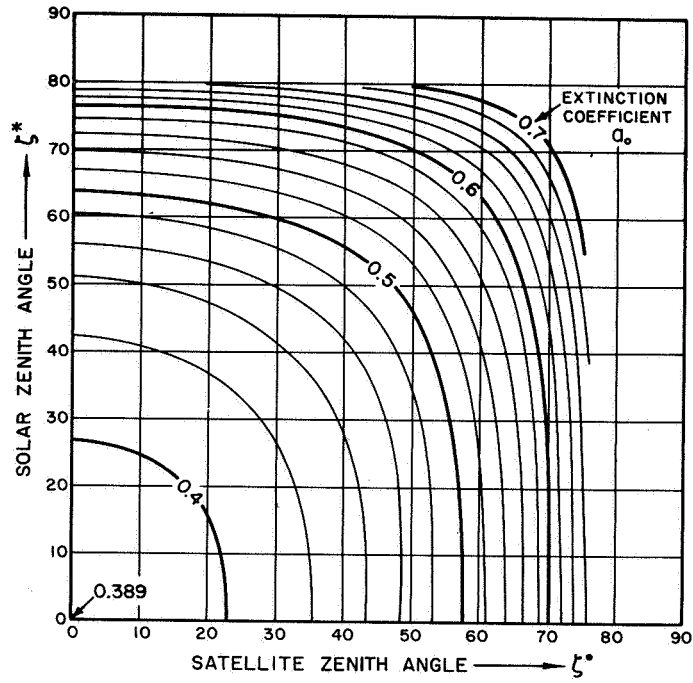


Fig. 3. A diagram to obtain Q_0 , the extinction coefficient at sea level, as a function of ζ^* and ζ° . The isolines were obtained by using Channel 3, floor sensor, TIROS III.

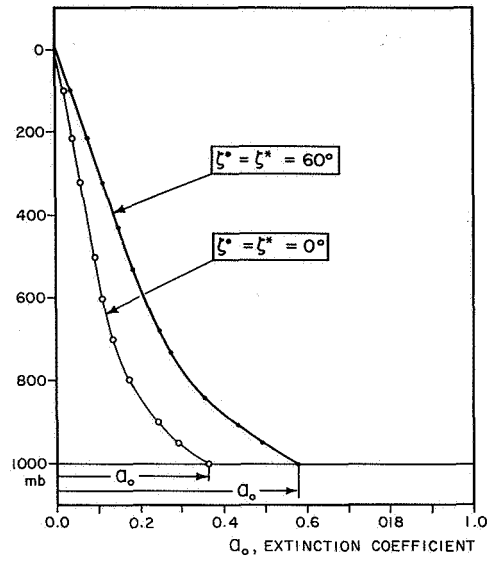


Fig. 4. Changes in the extinction coefficient when a reflecting surface was raised from 1000 mb to lower pressure altitudes. Two extreme cases of solar and satellite zenith angles are presented.

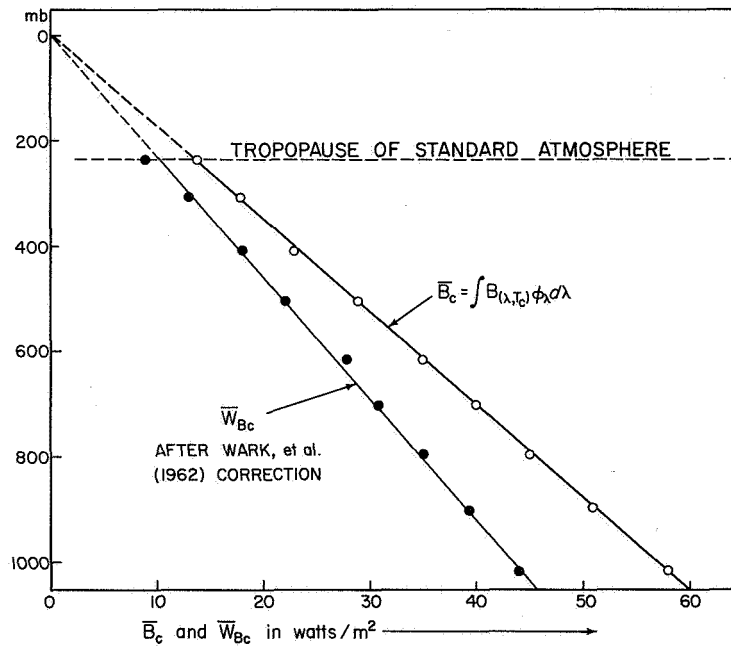


Fig. 5. Relationship between pressure and effective blackbody radiant emittance for TIROS channel 2 in the Standard Atmosphere.

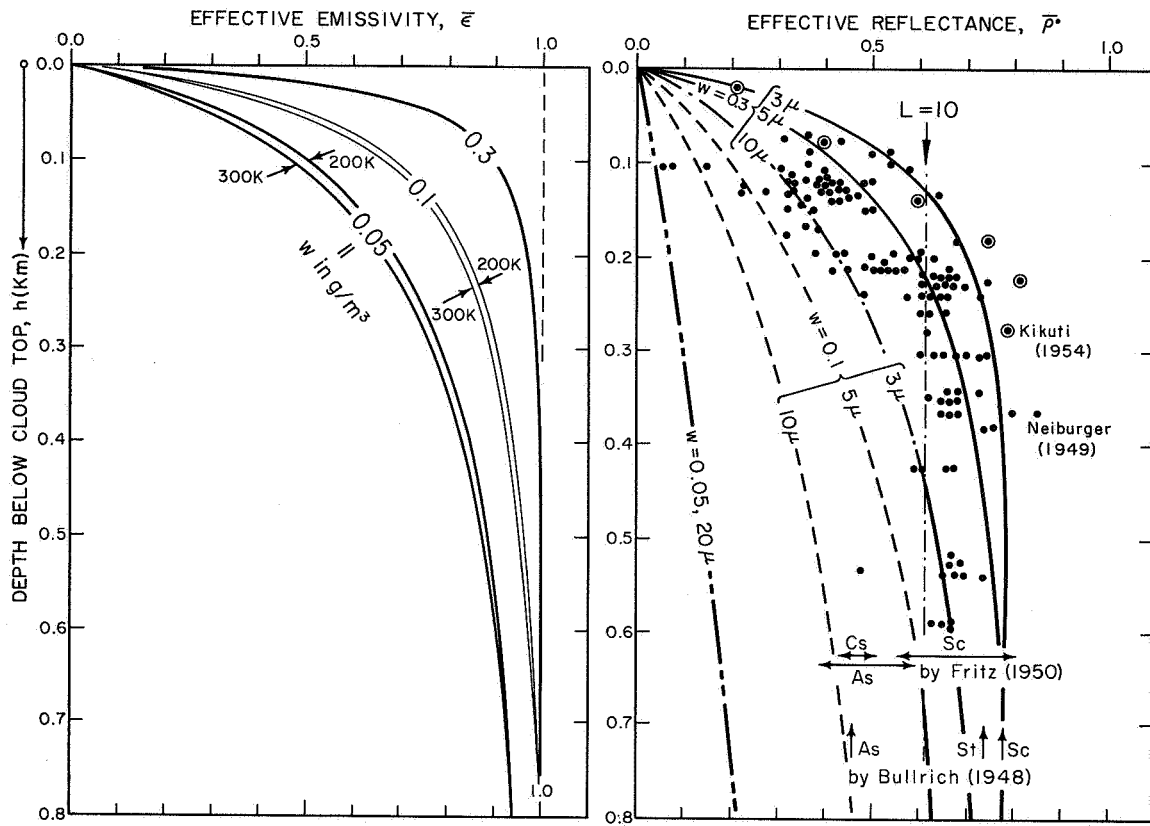


Fig. 6. Emissivity and reflectance of clouds as a function of cloud depth for different values of liquid water content and droplet radius.

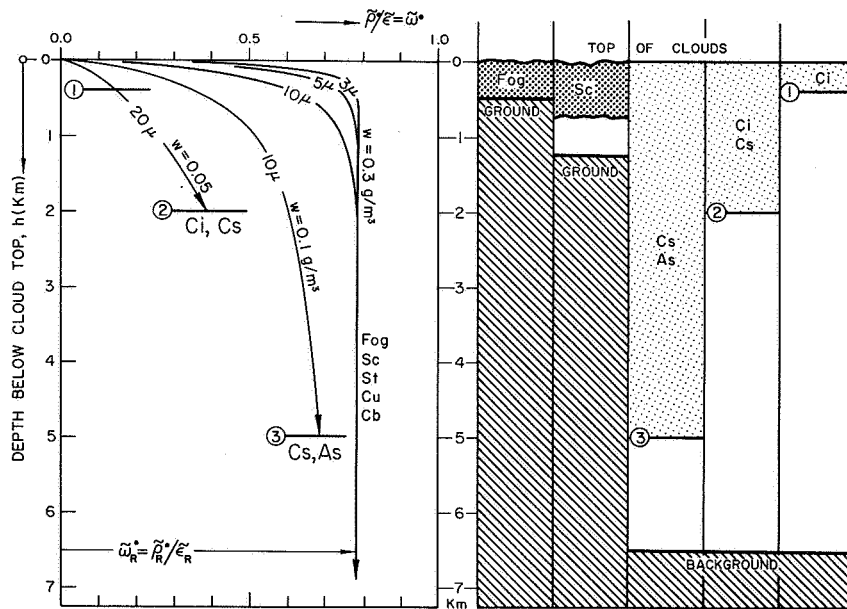


Fig. 7. Whiteness of clouds, $\tilde{\omega}_r$ as a function of cloud depth for different values of liquid water content and droplet radius.

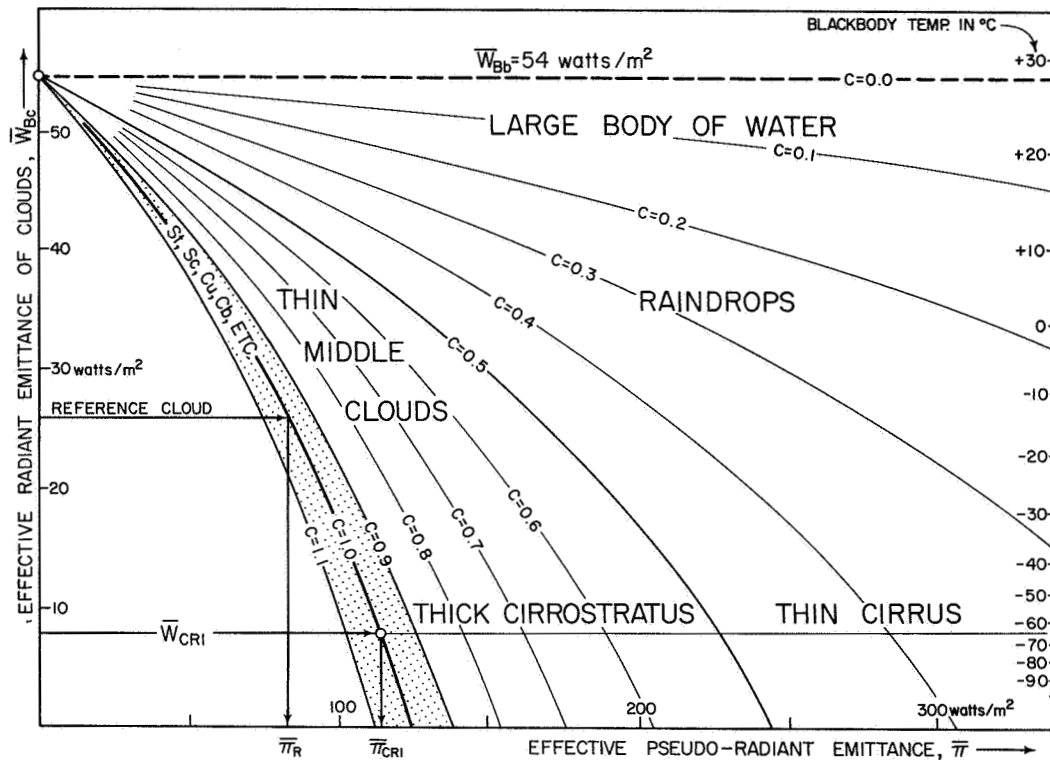


Fig. 8. Isolines of cloudiness, C , drawn on coordinates of effective radiant emittance, \bar{W}_e , and effective pseudo-radiant emittance, \bar{T} . The domain of reference clouds is indicated by the stippled area.

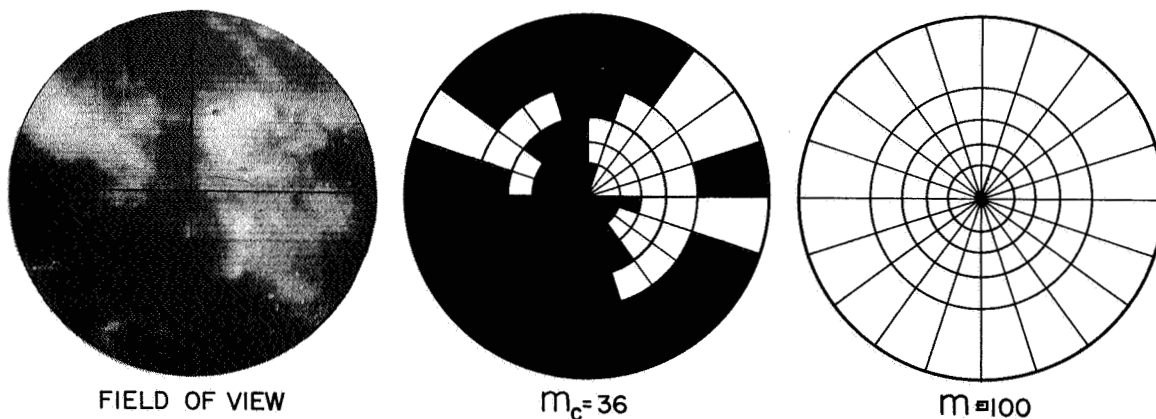


Fig. 9. Example of the computation of the photographic cloud cover, n_p , within the field of view of a radiometer.

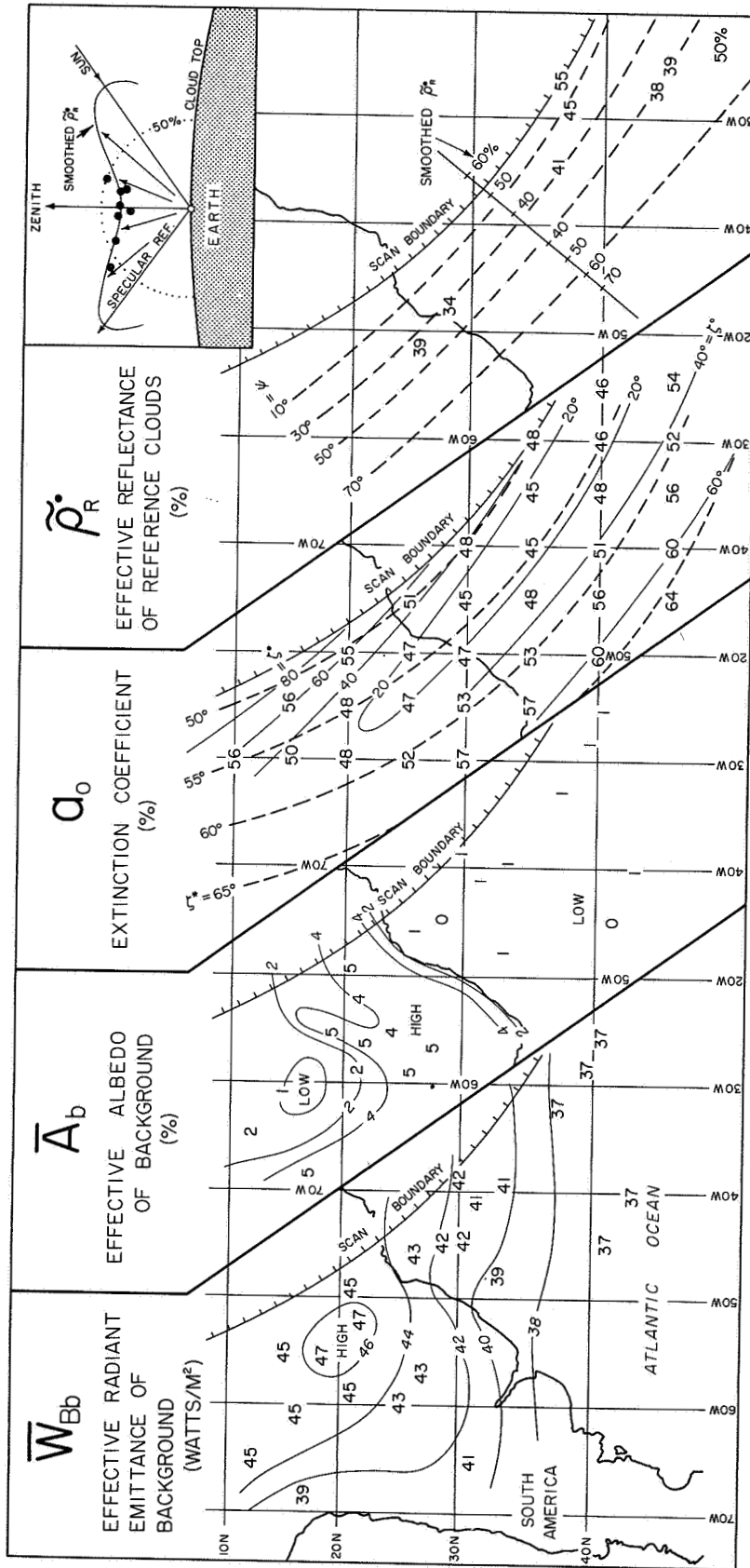


Fig. 10. An example of \bar{W}_{Bb} , \bar{A}_b , q_0 , and $\bar{\rho}_R$ fields for TIROS III, R/O 289 over South America and the southern Atlantic Ocean. Values in the \bar{W}_{Bb} and \bar{A}_b charts were obtained from Channel 2 and 3 radiation maps after identifying large clear areas in satellite cloud pictures covering the scan area. To indicate the fields of these values, they are contoured for every 2 watts m^2 of effective radiant emittance and for every 2% of effective reflectance. Values of q_0 were computed from solar zenith angles, ζ^* , and satellite zenith angles, ζ' , with the aid of Fig. 4. Isolines of these angles are shown by thin- and dashed-line contours. $\bar{\rho}_R$ was computed by using Eq. (55), which includes \bar{W}_{Bb} and q_0 , already known, and \bar{W} and \bar{A} , obtained from Channel 2 and 3 radiation maps over the areas of solid cloud cover. Included also in this chart are isolines of scattering angles, ψ , which vary between 6° and 96° within the scan area. When $\bar{\rho}_R$ is plotted as a function of ψ , as in the upper right, it is seen that it varies significantly as a function of ψ . In such a case, different $\bar{\rho}_R$ must be used at different geographic locations inside the scan area.

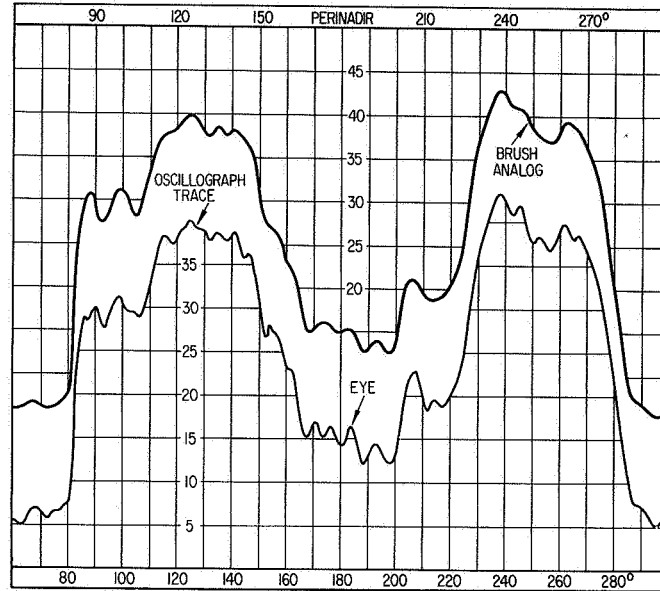


Fig. 11. Oscillograph and Brush Recorder analog traces from the region of Hurricane Anna of July 21, 1961, located near the perinadir. Horizontal and vertical scales denote the scan angle and the frequency, respectively. TIROS III, Orbit 132, R/O 133, Channel 2.

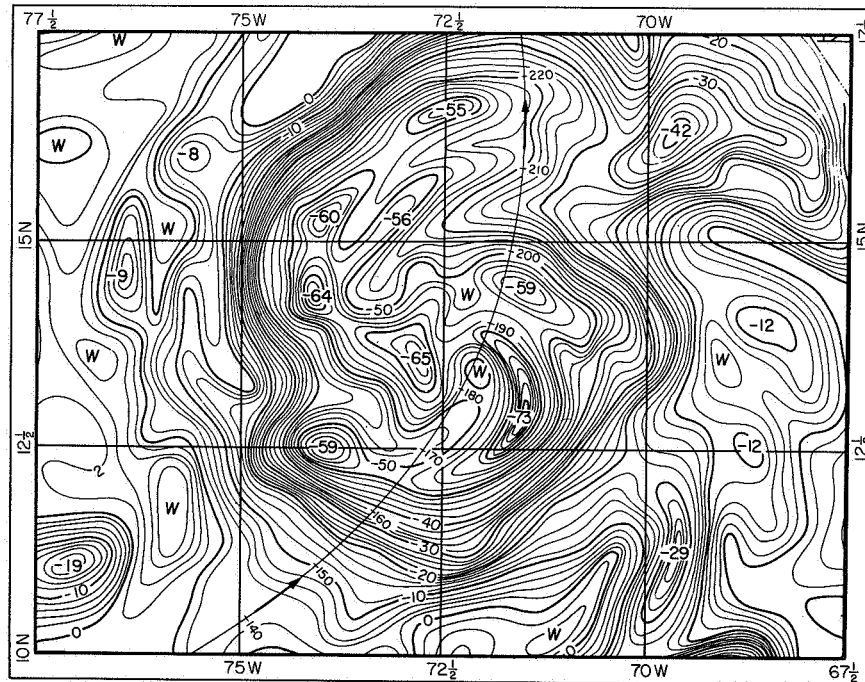


Fig. 12. One of the most detailed patterns of equivalent blackbody temperature of the cirrus shield of Hurricane Anna, obtained from Channel 2 radiation data. A scan line corresponding to the analog traces in Fig. 9 appears as a curved line accompanied by the scan angles at 10° intervals. The pattern was obtained by a Scanning Printer at the University of Chicago. TIROS III, Orbit 132, R/O 133.

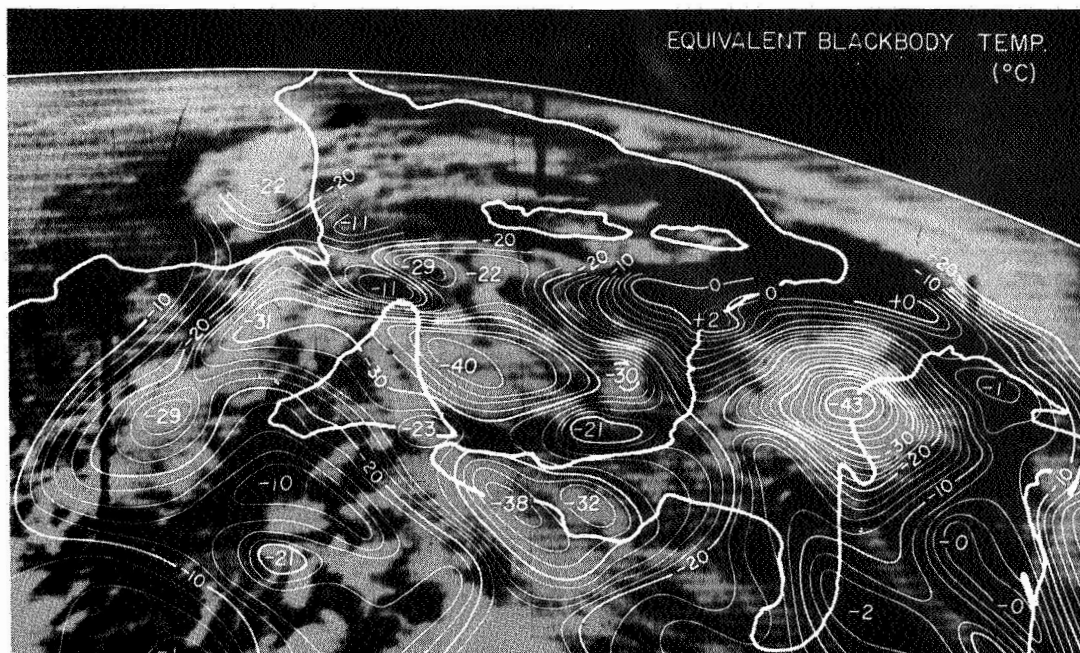


Fig. 13. Isotherms of the equivalent blackbody temperature superimposed upon a satellite picture within five minutes of the time of radiation measurement. TIROS IV, Orbit 99, Feb. 15, 1962. The picture covers the western Mediterranean.

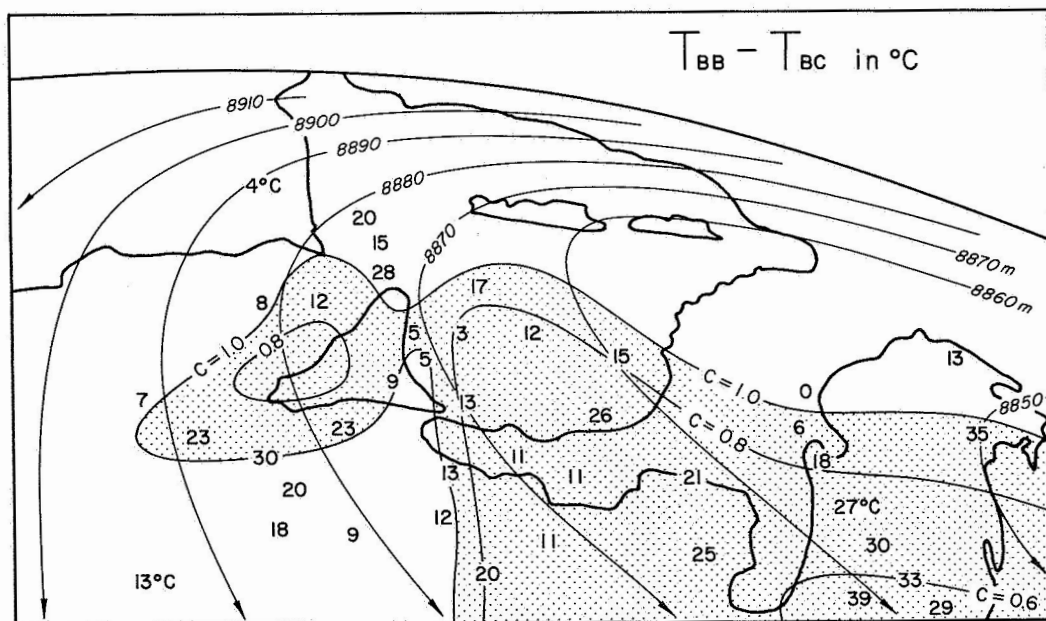


Fig. 14. The difference between the equivalent blackbody and the actual cloud-top temperatures. The former is always higher than the latter, due to the partial filling of scan spots by clouds. Low emissivity of the clouds also increases the difference. Isolines of the cloudiness, C , are drawn and the stippled area indicates values of $C < 1.0$. Thin lines with arrows indicate 300-mb contour map. TIROS IV, Orbit 99.

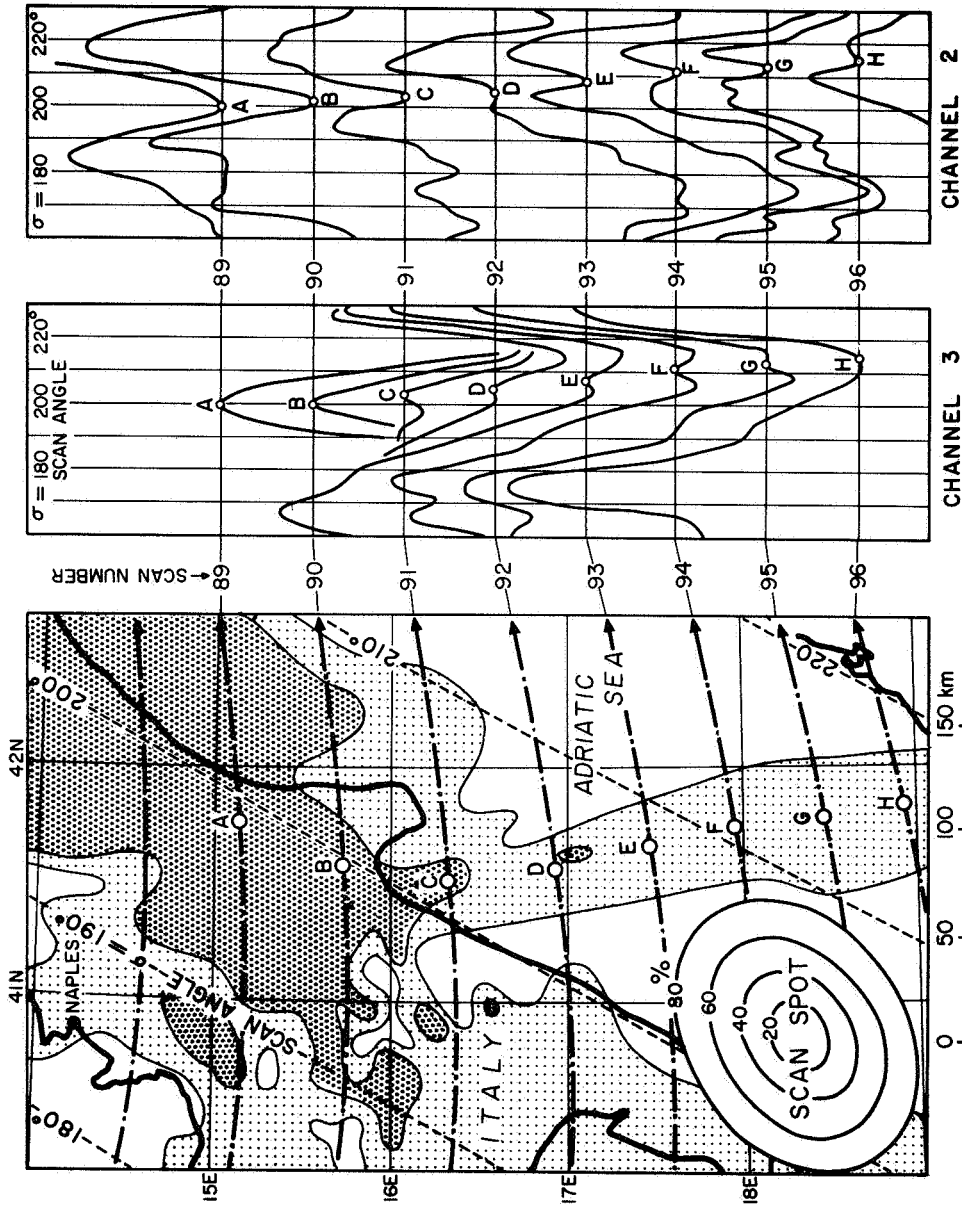


Fig. 15. Thunderstorm and anvil clouds expressed by two-tone stipplings and by a number of scan lines that crossed these clouds. Channel 2 and 3 analog traces to the right show a slight rise in reflectance and a drop in radiant emittance when the scan spot moved over the cloud axis. (TIROS IV, Orbit 99.)

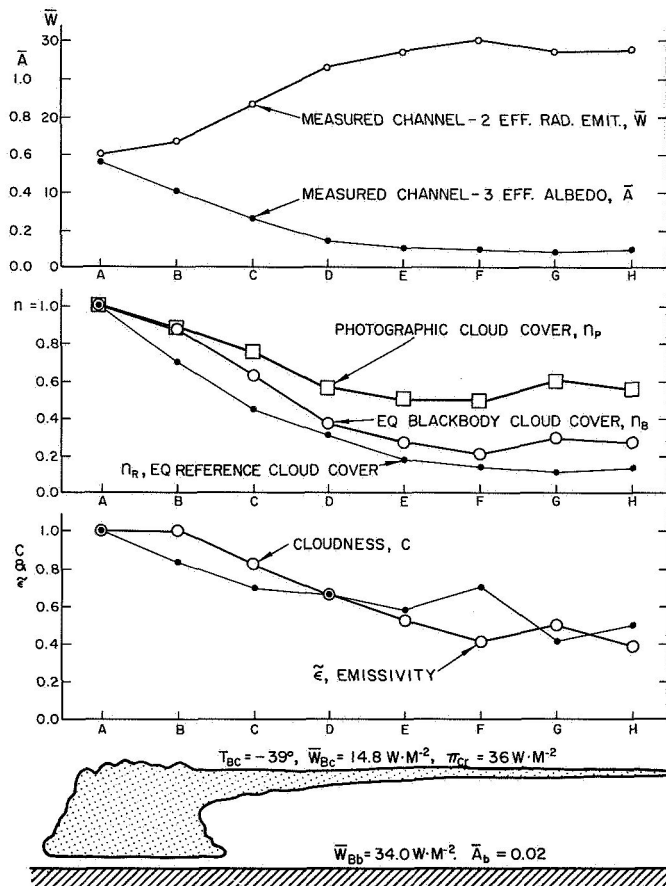


Fig. 16. Cloud parameters computed from long- and short-wave radiation data shown in the previous figure. These parameters have not been completely interpreted, since they are very sensitive to the physical properties of the anvil cloud undergoing a slow evolution.

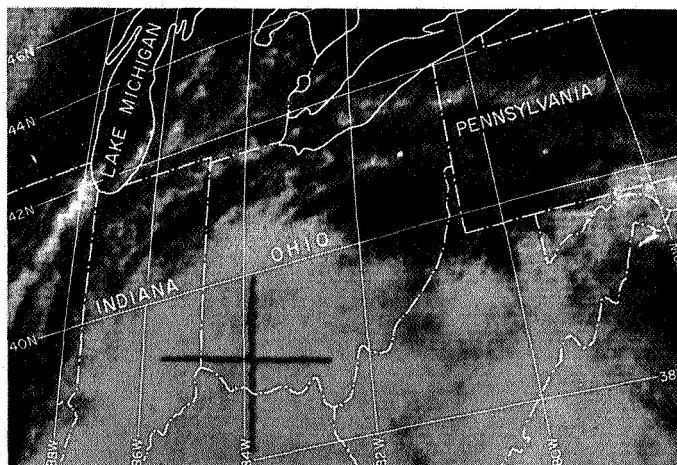


Fig. 17. Gridded picture from TIROS III, R/O 004, 1734 GMT, July 12, 1961.

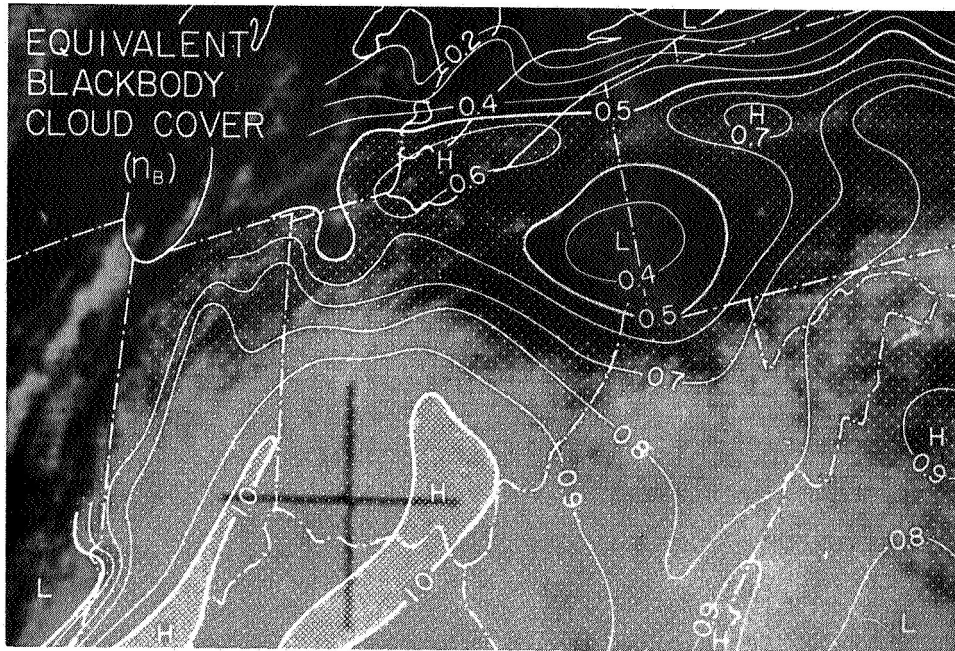


Fig. 18. Isolines of equivalent blackbody cloud cover drawn on coordinates of the satellite picture of Fig. 17. (TIROS III, R/O 004).

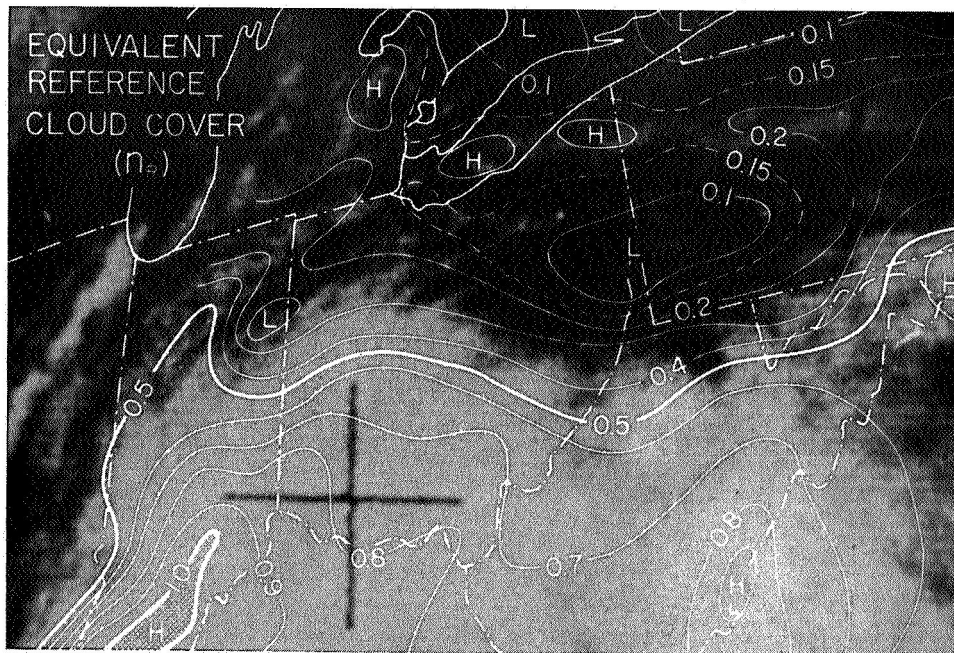


Fig. 19. Isolines of equivalent reference cloud cover drawn on coordinates of the satellite picture of Fig. 17. (TIROS III, R/O 004).

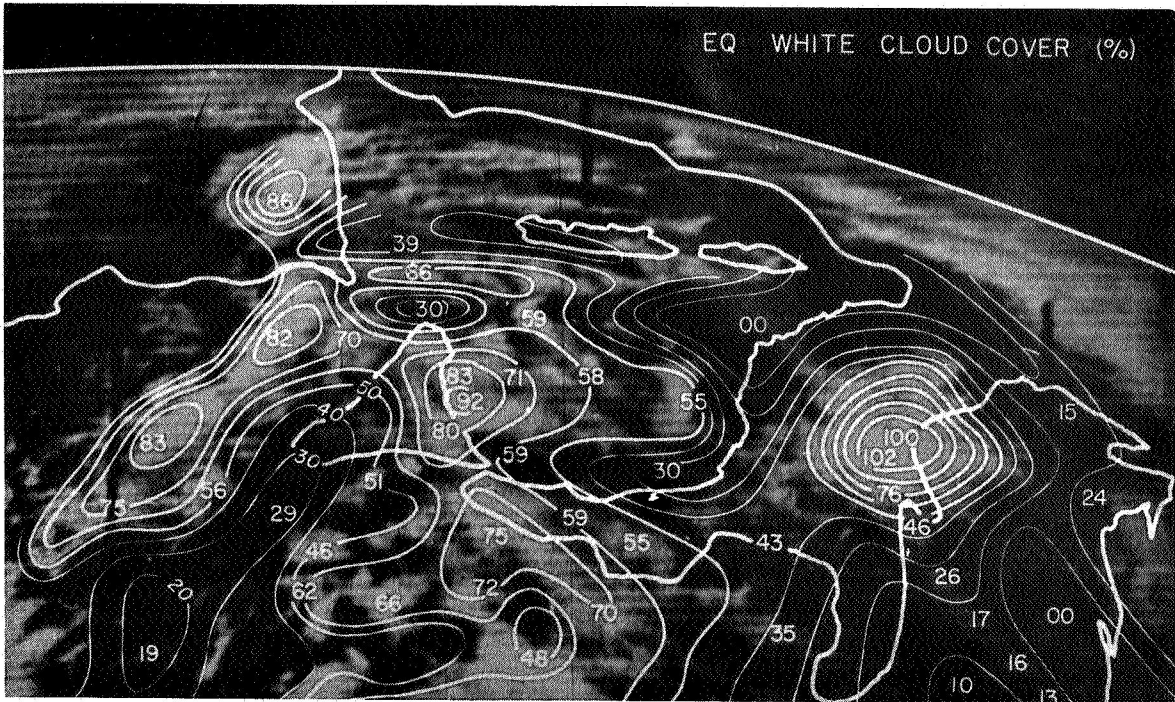


Fig. 20. Isolines of equivalent reference cloud cover on coordinates of the satellite picture of Fig. 13. (TIROS IV, Orbit 99).

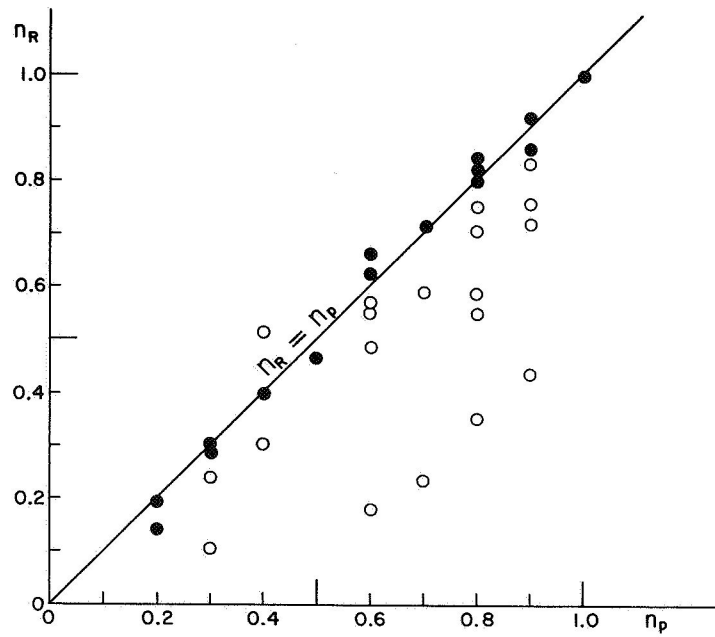


Fig. 21. Scatter diagram of equivalent reference cloud cover versus photographic cloud cover. Non-cirrifiform clouds are indicated by black dots. (TIROS IV, Orbit 99.)

MESOMETEOROLOGY PROJECT - - - RESEARCH PAPERS

(Continued from front cover)

42. A Study of Factors Contributing to Dissipation of Energy in a Developing Cumulonimbus - Rodger A. Brown and Tetsuya Fujita
43. A Program for Computer Gridding of Satellite Photographs for Mesoscale Research - William D. Bonner
44. Comparison of Grassland Surface Temperatures Measured by TIROS VII and Airborne Radiometers under Clear Sky and Cirriform Cloud Conditions - Ronald M. Reap
45. Death Valley Temperature Analysis Utilizing Nimbus I Infrared Data and Ground-Based Measurements - Ronald M. Reap and Tetsuya Fujita
46. On the "Thunderstorm - High Controversy" - Rodger A. Brown
47. Application of Precise Fujita Method on Nimbus I Photo Gridding - Lt. Cmd. Ruben Nasta